

Observed Variability of Ocean Wave Stokes Drift, and the Eulerian Response to Passing Groups

JEROME A. SMITH

Scripps Institution of Oceanography, La Jolla, California

(Manuscript received 4 January 2005, in final form 13 September 2005)

ABSTRACT

Waves and currents interact via exchanges of mass and momentum. The mass and momentum fluxes associated with surface waves are closely linked to their Stokes drift. Both the variability of the Stokes drift and the corresponding response of the underlying flow are important in a wide range of contexts. Three methods are developed and implemented to evaluate Stokes drift from a recently gathered oceanic dataset, involving surface velocities measured continually over an area 1.5 km in radius by 45°. The estimated Stokes drift varies significantly, in line with the occurrence of compact wave groups, resulting in highly intermittent maxima. One method also provides currents at a fixed level (Eulerian velocities). It is found that Eulerian counterflows occur that completely cancel the Stokes drift variations at the surface. Thus, the estimated Lagrangian surface flow has no discernable mean response to wave group passage. This response is larger than anticipated and is hard to reconcile with current theory.

1. Introduction

Surface waves are of central importance in general to air–sea interactions (Thorpe 1982; Edson and Fairall 1994; Andreas et al. 1995; Asher et al. 1996; Pattison and Belcher 1999; Zilitinkevich et al. 2001; Zappa et al. 2004), and in particular to the motion in the surface layer of the sea. For example, much of the wind stress acts directly on the waves, which then transmit the stress to the underlying flow via intermittent wave-breaking events. Although they have historically been the subject of much discussion, the implications of this intermittent stress transfer have only recently been simulated and studied in detail (Sullivan et al. 2004). The simulations indicate that vortical structures resulting from breaking events influence the motion to a depth many times as great as the wave amplitude, deeper than previously thought.

It has long been recognized that waves transport mass and momentum (Stokes 1847; Longuet-Higgins 1953). Both are related to the difference between the average velocity of a fluid parcel (Lagrangian velocity) and the current measured at a fixed point (Eulerian

velocity). This difference, first identified by Stokes (1847), is called the “Stokes drift.” The vertical integral of the Stokes drift is the “Stokes transport,” corresponding to both the net mass flux and wave momentum per square meter of the surface (Longuet-Higgins and Stewart 1962). Because waves are strained and refracted by currents, exchanges of mass and momentum occur between the waves and mean flow. Longuet-Higgins and Stewart (1962, 1964), described the “excess flux of momentum due to the presence of waves” and, in analogy to optics, named it the “radiation stress” (noting a slight grammatical inconsistency, but bowing to historical usage). Changes in the radiation stress (momentum flux) of the waves are compensated for by changes in the mean field, so the overall momentum is conserved. Additional analysis is needed to determine the partitioning of momentum between waves and the mean. For example, earlier papers (Longuet-Higgins and Stewart 1960, 1961) provided the basis for the description of the generation of group-bound forced long waves, which is relevant to the “Eulerian response” discussed here. Such wave–current interactions are also considered important in generating and maintaining Langmuir circulation (LC), a prominent form of motion found in the wind-driven surface mixed layer (Langmuir 1938; Craik and Leibovich 1976; Craik 1977; Leibovich 1977, 1980; Phillips 2002). Analyses and simulations indicate that LC is important in the long-

Corresponding author address: Dr. J. A. Smith, Scripps Institution of Oceanography, UCSD, Mail Stop 0213, 9500 Gilman Dr., La Jolla, CA 92093-0213.
E-mail: jasmith@ucsd.edu

term evolution of the mixed layer (Li et al. 1995; Skillingstad and Denbo 1995; McWilliams et al. 1997; McWilliams and Sullivan 2000). A key term in the generating interaction involves the bending of vortex lines by the vertically nonuniform Stokes drift of the waves.

For depth-resolving simulations, the depth dependence of the Stokes drift, including variations in direction as well as magnitude, is needed.

To date, analyses and simulations of Langmuir circulation have considered only an overall mean (temporal and horizontal) Stokes drift resulting from the waves. However, given that the intermittent nature of wave breaking in transmitting stress to the underlying flow has recently been found to be important (Sullivan et al. 2004), it is reasonable to examine the spatial and temporal scales over which the Stokes drift varies, because there may be an analogous effect.

Evaluation of Stokes drift from a recently gathered oceanic dataset is one focus of this paper. The experiment took place just off the west-northwest shore of Oahu (Hawaii). An area of the ocean surface with a roughly 1.5 km radius by 45° in bearing was monitored for velocity and acoustic backscatter intensity, using a novel acoustic Doppler system referred to as the “long-range phased-array Doppler sonar” (“LRPADS”). The area is resolved to 7.5 m in range by 1.3° in bearing (~7000 cells), sampled every 2.5 s. The vertical aperture encompasses the ocean surface and the near-surface bubble layer, which almost always dominates in backscatter intensity by several orders of magnitude over returns from all other depths, and yields a vertical-scale depth for the measurement of about 1.5 m.

Another focus is the examination of the underlying flow field. One method developed here for the Stokes drift (“method 3”) involves estimating currents at both a fixed level (Eulerian) and following the surface (semi-Lagrangian: following vertical but not horizontal displacements). It is found that Eulerian counterflows occur that cancel the estimated Stokes drift variations at the surface completely. This is a stronger surface response than expected from the group-bound forced wave analysis mentioned above (discussed further in section 7).

The observations presented here are the first concerning the Eulerian surface current response to short-wave groups in open-ocean, deep-water conditions (>1000 m depth). Wave group responses in the field have been observed previously via pressure arrays in intermediate-depth water (Herbers et al. 1994), and were found to be consistent with second-order theory for that case. However, the expected response in intermediate depths differs markedly from that in deep water, and the measurements were close to the bottom

rather than near surface, so a detailed comparison is not appropriate.

Similarly sized Eulerian counterflows have also been observed in laboratory experiments (Kemp and Simons 1982, 1983; Jiang and Street 1991; Nepf 1992; S. G. Monismith et al. 1996, unpublished manuscript; Groeneweg and Klopman 1998; Swan et al. 2001). The changes in the Eulerian current profile from case to case (no waves, down-current waves, up-current waves) are comparable to (and oppose) the Stokes drift profile calculated from the wave parameters as given (in both magnitude and shape). However, in these experiments the waves are quasi steady, and there is time for the turbulence to adjust over the depth of the waves. Indeed, this is the interpretation given for numerical simulations of these cases (Groeneweg and Klopman 1998; Huang and Mei 2003). In contrast, the field observations described here involve short groups or “packets” of waves, and the response occurs too quickly for the diffusion of vorticity to occur; thus, the results are puzzling and remain to be explained satisfactorily.

The vertical structures of the Stokes drift and Eulerian response are not discussed here. While the profile of Stokes drift can be estimated from the directional wave parameters, the vertical profile of the Eulerian response is not resolved in this dataset. Only the values near the surface (averaged over the near-surface bubble layer) are observed, compared, and discussed here.

Organization of the paper is as follows. Stokes transport and drift are defined in section 2, with an eye toward evaluation from measured directional wave spectra. The experimental setting and circumstances are described in section 3. In section 4, an area-mean estimate of Stokes drift at the surface is described that is based on the difference between the mean velocity of features embedded in the flow (bubble clouds) versus the mean Doppler shift; this also introduces consideration of acoustic sheltering by wave crests. In section 5, two more methods are developed to estimate Stokes drift, using wavenumber–frequency (k – f) Fourier coefficients of the time–range data. The Eulerian and Lagrangian responses are evaluated in section 6, following the method outlined in section 5. Discussion of the results versus the expected irrotational response is in section 7. Results and conclusions are summarized in section 8.

2. Stokes drift resulting from the surface waves

To set the stage and clarify terminology, the Stokes drift is defined and some of its characteristics are described for the case of deep-water surface waves. Both

the volume transport and the Stokes drift profile resulting from the presence of waves are considered, and the stage is set to estimate the time–space variations of Stokes drift and transport from data.

a. Stokes transport and linear waves

In an Eulerian frame, the Stokes transport arises entirely at the moving surface. For simplicity, the density is assumed constant, and is set to 1. Taylor expanding from the mean surface at $z = 0$ is

$$\begin{aligned} \mathbf{T}^S &\equiv \int_{-h}^{\zeta} \mathbf{u}(z) dz - \int_{-h}^0 \mathbf{u}(z) dz \\ &\approx \left(\overline{\zeta \mathbf{u}'} + \frac{1}{2} \overline{\zeta^2 \partial_z \mathbf{u}} + \dots \right)_{z=0}. \end{aligned} \tag{2.1}$$

The mean vertical shear is assumed to be small, leaving just the first term on the right. The linearized momentum equation at the surface, again expanding from $z = 0$, is used to complete the evaluation. Aligning the wave with the x axis so that $\mathbf{u} = u$, and substituting a wave solution of the form $P e^{i(kx - \sigma t)}$ for both ζ and u ,

$$\partial_t u + g \partial_x \zeta = (-i\sigma)u + g(ik)\zeta \quad \text{or} \quad u = \sigma \zeta, \tag{2.2}$$

where use is made of the linear dispersion relation in the absence of currents, $\sigma^2 = gk$. Thus, the net Stokes transport is

$$\mathbf{T}^S \approx \overline{\zeta u} = \sigma \overline{\zeta^2} = \overline{u^2} / \sigma. \tag{2.3}$$

For waves propagating in weak shear, the Stokes transport can be identified to second order in wave slope with the wave momentum.

b. Stokes drift profile

Theories describing wave–current interactions generally require not just the integrated transport, but also the vertical profile of Stokes drift. To determine this, the notion of “displacement” is extended to the fluid interior, and also to include the horizontal displacements associated with the waves. The displaced location of a fluid parcel is associated with its undisplaced location; that is, for some function of space–time “ q ,” associate

$$q^L(x, z, t) \Leftrightarrow q(x + \chi, z + \zeta, t) \tag{2.4}$$

following Andrews and McIntyre (1978) (note there is an implicit assumption that the mapping is unique and invertible; also, the Jacobean of this transformation might not be one).

The generalized Lagrangian mean (GLM; cf. Andrews and McIntyre 1978) is formed over the displaced

locations, while the Eulerian mean is formed (as is normally done) at the undisplaced location,

$$\begin{aligned} \overline{q}^L &= \overline{q(x + \chi, z + \zeta, t)} \quad \text{and} \\ \overline{q}^E &= \overline{q(x, z, t)} = \overline{q}. \end{aligned} \tag{2.5}$$

The Stokes drift associated with the waves is the difference between the GLM and Eulerian mean velocities,

$$\overline{u}^S \equiv \overline{u}^L - \overline{u}^E. \tag{2.6}$$

Consider next the instantaneous difference between the horizontal velocity at the displaced minus undisplaced locations,

$$\begin{aligned} u^{IS} &\equiv u(x + \chi, z + \zeta, t) - u(x, z, t) \\ &\approx (\chi \partial_x u + \zeta \partial_z u)_{(x,y,t)} + (\text{H.O.}). \end{aligned} \tag{2.7}$$

For a monochromatic small-amplitude wave in deep water, the velocity field can be written as

$$u(x, z, t) = \text{Re}[U(x, z, t)] = \text{Re}[P_u(k, \sigma) e^{kz} e^{i(kx - \sigma t)}], \tag{2.8}$$

where P_u is a complex velocity amplitude (like a single Fourier component). The horizontal displacement field is a time integral of horizontal velocity,

$$\chi = \int_{t_0}^t u dt = \text{Re}[(-i\sigma)^{-1} U] = -\sigma^{-1} \text{Im}(U), \tag{2.9}$$

and the vertical displacement field is

$$\zeta = \sigma^{-1} \text{Re}(U). \tag{2.10}$$

The velocity gradients are

$$\begin{aligned} \partial_x u &= \text{Re}[(ik)U] = -k \text{Im}(U) \quad \text{and} \\ \partial_z u &= \text{Re}[(k)U] = k \text{Re}(U). \end{aligned} \tag{2.11}$$

To second order in wave steepness, the instantaneous Stokes drift is

$$u^{IS} \approx (\chi \partial_x u + \zeta \partial_z u)_{(x,y,t)} = (k/\sigma)(u^2 + w^2) = |U|^2/c. \tag{2.12}$$

Note that one-half of the net Stokes drift comes from the vertical displacements, and half from the horizontal (in deep water). As an aside, note also that this instantaneous drift is constant with respect to the wave phase for deep-water waves, where the orbital motions are circular.

The above considers a single-wave component. For a spectrum of waves, the nonlinearity of (2.7) or (2.12) means that shorter waves riding on longer ones introduce high-frequency oscillations to $|U|$, so some form of wave filtering is required. This is addressed in section 5, where methods are developed to use wavenumber–

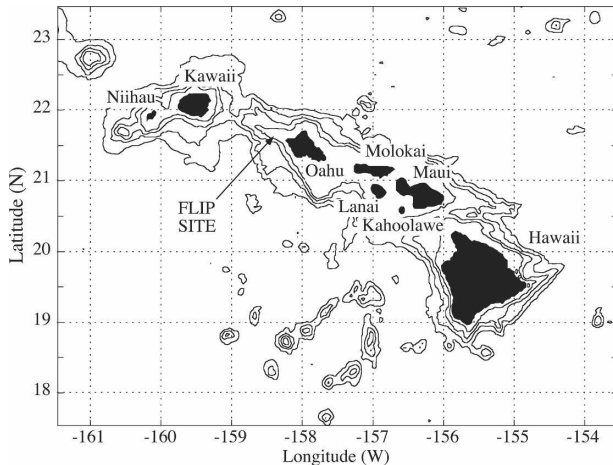


FIG. 1. Location of R/P *FLIP* during the near-field leg of HOME, from September through October 2002. The site is about 30 km east–northeast of Oahu, over an underwater ridge that extends roughly halfway to Kauai. The depth contour interval is 1000 m, with the deepest shown at 4000 m. (The abyssal plain is 5000 m, so that contour is messy and hence is omitted.) Data contoured are 2-min resolution, from National Geophysical Data Center (NGDC).

frequency Fourier coefficients to estimate the Stokes drift as well as to implement a wave filter. It remains true for multiple deep-water waves that half of the net Stokes drift derives from vertical and half from horizontal displacements.

Before proceeding with estimates of the time–space characteristics of the Stokes drift, the experimental setting and data collection is described. Then, an estimate of the global-averaged Stokes drift used previously is reexamined, leading to detailed consideration of the effects of the wave displacements on the measurements themselves, and also helping to motivate the wavenumber–frequency analysis that follows.

3. Experimental setting

The data considered here were gathered aboard the Research Platform (R/P) *Floating Instrument Platform (FLIP)*, in conjunction with the Hawaii Ocean Mixing Experiment (HOME; see Rudnick et al. 2003), at a location just west–northwest of Oahu (Fig. 1). Typical conditions there consist of steady trade winds of 10–12 m s^{-1} from the east, with occasional storms or calm periods. During the data-gathering period, the initially typical winds dropped, remained slack for a few days, and then resumed. Surface currents are dominated by tides, which cycled from spring to neap to spring tide again. The surface wave field varied from being strongly bimodal (or multimodal; i.e., distinct wave

groups from several directions) to approximately unimodal (a single dominant direction and peak frequency).

A key ingredient in current theories of LC generation is the Stokes drift profile resulting from surface waves (as noted above). Quantitative estimation of the Stokes drift requires good wave data: direction and frequency must be resolved over a wide range of scales. To provide this, a 50-kHz LRPADS was operated continuously for about 20 days, from 14 September to 5 October 2002. This provides both the surface waves and the underlying surface flows over a considerable area, with continuous coverage in both space and time.

The operating principles and concerns for a phased-array Doppler sonar are described by Smith (2002). In brief, an acoustic signal is transmitted in a broad horizontal fan, with a vertical beamwidth sufficient to encounter the surface beginning a few tens of meters away, and continuing until attenuation reduces the backscattered signal level below the ambient noise. The near surface is a region of strong backscatter. Bubbles, when present, provide backscatter that is of order 10^4 times louder than that from other scatterers. In the absence of bubbles, materials at the surface still often produce a signal stronger than that of the volume scatterer from below. Thus, the backscatter can for the most part be considered to be from the surface. Because the sample volumes are strongly surface trapped, the acoustic sheltering of wave crests by closer troughs is an aspect to be considered (see section 4). The backscattered signal is received on a linear transducer array and is digitally beamformed into an array of angles spanning the breadth of the transmitted fan. The time of flight since transmission is combined with the speed of sound to determine the range. The bulk of the acoustic paths are below the bubble layer, so sound speed variations are small, and a value based on the mean temperature and salinity in the surface mixed layer can be used. The returns are segmented in both range and angle, so each “ping” results in many measurements distributed over a pie-shaped surface area. For the LRPADS as configured in HOME, an area extending roughly 1.5 km in range and 45° in bearing is segmented into measurement bins about 1.3° wide (35 beams) and 7.5 m in range (200 range bins), with a total of 7000 locations. The entire area is sampled every 2.5 s (the time needed for sound to propagate out 1800 m and back) over the whole 20-day period (with few gaps, the largest of which are a few minutes long). The LRPADS was operated with about 7 kHz of usable bandwidth. Repeat-sequence codes (Pinkel and Smith 1992) were used to reduce Doppler noise, resulting in single-ping

rms noise levels of about 10 cm s^{-1} per range/angle bin. With 7-kHz bandwidth and 50-kHz center frequency, the code bits correspond to about seven wave cycles each. A plane wave from the outermost angles ($\pm 22^\circ$) completes 16 cycles across the face of the receiver array, corresponding to more than two bit's worth; thus, beam forming is done via time delay. While this is more computationally demanding than simple FFT beam forming, it also reduces the ambiguity between the Nyquist wavenumber angles (between $+22^\circ$ and -22°). As operated, the selectivity between $+22^\circ$ and -22° for the LRPADS in HOME appears empirically to be of the order of 6 dB. The continuous data stream was segmented into files of about 8.5 min worth each. Retaining raw data permits experimentation with new beam-forming algorithms, near-field focusing, and/or resampling with a higher range resolution.

The Doppler shift is estimated with a time-lagged covariance technique (Rummler 1968), where each ping is considered independently. With this scheme, there is a finite level of Doppler noise even at a high signal-to-noise ratio (SNR; see Theriault 1986; Brumley et al. 1991; Pinkel and Smith 1992; Trevorrow and Farmer 1992). At the farthest ranges, the SNR decreases as the signal fades into the ambient acoustic noise, further degrading the estimates. For finite SNR, use is made of the empirical finding (Pinkel and Smith 1992) that the error variance e_σ^2 of the Doppler-shifted frequency estimate is about twice the value of the lower bound given by (Theriault 1986)

$$e_\sigma^2 \approx \frac{2}{LT_a T_o} \left(1 + \frac{36}{\text{SNR}} + \frac{30}{\text{SNR}^2} \right), \quad (3.1)$$

where L is the number of independent samples (here, the number of bits in the repeated code), T_o is the duration of the total transmitted code sequence less covariance lag time (“overlap time”), and T_a is the averaging window length (Smith 2002). The measured backscatter intensity is used to estimate the SNR, assuming that the farthest ranges contain only noise. To facilitate objective viewing and to precondition the data for Fourier analysis, the velocity estimates are scaled to make the net error variance constant with range; that is, they are divided by the square root of the portion in parentheses in (3.1). As a consequence, the values at the farthest ranges, where the signal approaches pure noise, are tapered smoothly to zero.

Example single-ping frames from sequences of slope and elevation images are shown in Fig. 2. The spatial dynamic range of the measurements is illustrated by the following combination: wavelengths from about 15 m to

over 1 km are resolved, corresponding to wave periods from 3 to more than 20 s, longer than any swell in this dataset. The full three-dimensional (two space + time) evolution of the surface velocity fields can be viewed in the form of movies, or various slices through the 3D data volume or corresponding 3D spectra can be considered.

4. Area-mean velocities and acoustic sheltering

The most direct way to estimate the Stokes drift is to simultaneously measure a Lagrangian mean and the corresponding Eulerian mean velocities. Two area-mean velocity estimates can be formed from LRPADS data that tend toward this ideal, but fall short. The two estimates arise from 1) the area-mean displacement of all intensity features from one time to another (Smith 1998), and 2) weighted averages of the Doppler shifts over the area, yielding mean along-axis (cosine weighted) and across-axis (sine weighted) velocity components (where the “axis” is the center angle of the beam-formed array). The first, based on an area-mean feature-tracking algorithm, is a Lagrangian velocity estimate. The other, based on mean Doppler shifts, is not exactly Eulerian or Lagrangian, but something in between. This requires further analysis to be understood, and a few assumptions for quantitative evaluation (see below), but also leads to a more accurate way to estimate Stokes drift and other effects. Nevertheless, the difference between the two area-mean velocities is a reasonable approximation of the Stokes drift, within 25%, as will be seen. This area-mean approach is “method 1” for the estimation of Stokes drift.

Development of the feature-tracking average arose from an unrelated motivation: simple time averaging to eliminate surface waves can lead to significant smearing of features resulting from advection by the mean flow. The area-mean feature-tracking algorithm is described by Smith (1998). A fringe benefit is estimation of an area-mean horizontal Lagrangian velocity. An alternative is to form averages moving with the mean velocity derived from the Doppler signal; however, the two differ systematically, and the former maintains sharper features. Smith (1998) noted that the difference between the two mean velocities corresponds closely to the Stokes drift calculated from a resistance wire (surface elevation) directional wave sensing array using second-order quantities derived from linear wave theory (as in section 2). The feature-tracking algorithm was applied to the HOME LRPADS dataset. Figure 3 shows a comparison of the velocity difference [feature track–Doppler velocity (FDV)] versus a rule-of-thumb

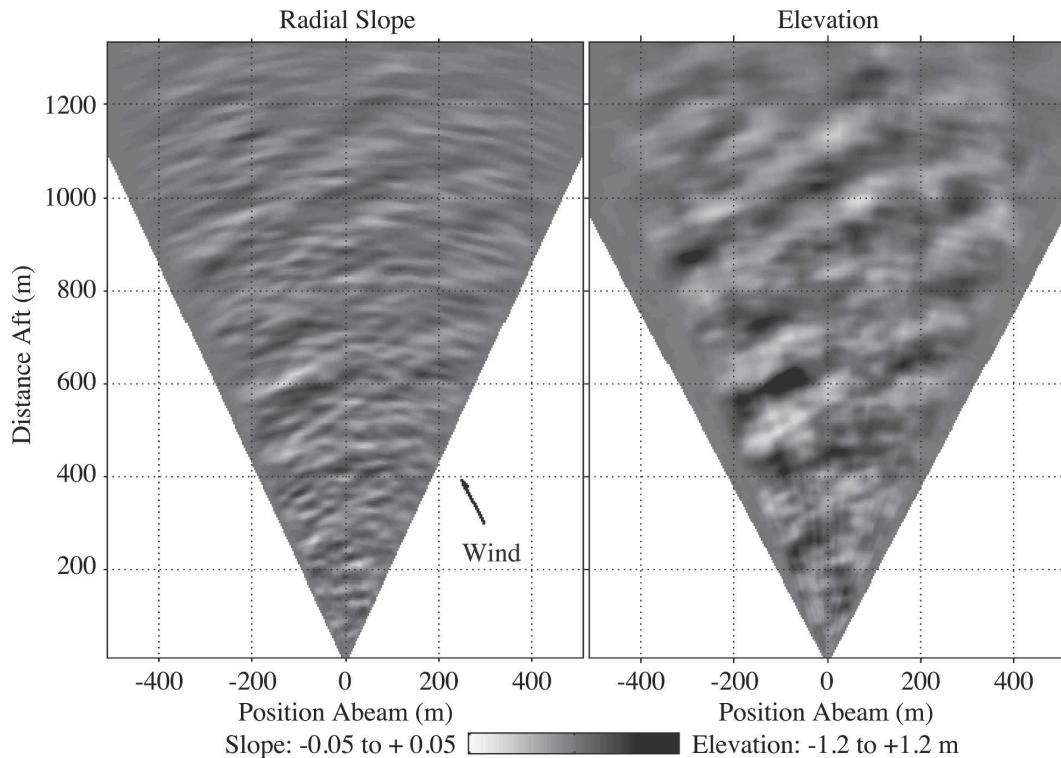


FIG. 2. Two views of the surface wave field: (left) radial slope component and (right) estimated surface elevation. The black arrow indicates the wind direction and magnitude ($\sim 10 \text{ m s}^{-1}$). The dominant waves are near 10-s period, and are propagating downwind. In the elevation plot (right) some weaker wave components can be seen propagating to the right, with crests roughly parallel to the left edge of the pie. Data are from 1453 Hawaii daylight savings time (HDT) 4 Oct 2002.

estimate that the Stokes drift is 1%–2% of the wind speed [note that the appropriate comparison is not with the Stokes drift at the actual surface, but with a “bubble-weighted average” over the top few meters as discussed below; e.g., see discussion after (5.18)]. The best match occurs for 1.25% W_{10} , which is within this range. It is also seen that the difference vector is roughly parallel to the wind. As an aside, note that while the overall agreement on longer time scales between the FDV and 1.25% W_{10} is quite close, the two vary out of phase with approximately the tidal frequency over the later windy period (yeardays 272–276). This suggests that the waves respond to the large-scale currents associated with the tides in addition to the local wind. Investigation of this is suggested for future work.

The measurements can be understood as vertical as well as horizontal averages, with the depth averaging determined by the vertical distribution of bubbles (which are the dominant scatterers). The feature-tracking velocities are estimates of the mean bubble advection. Because the bubbles are embedded in the fluid, and both the rise-rate and the macroscopic evo-

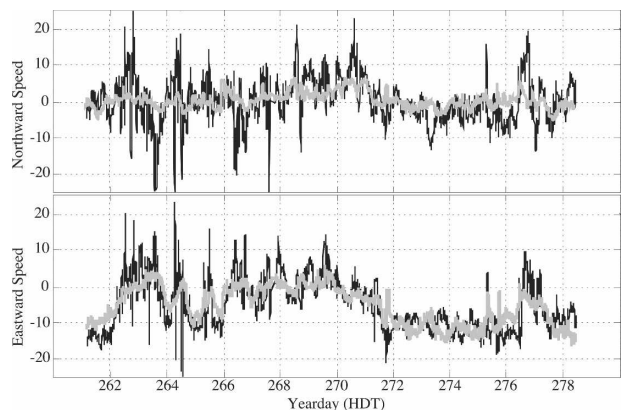


FIG. 3. Feature-tracking minus Doppler-based velocity estimates ($V_{\text{feature}} - V_{\text{Doppler}}$ or “FDV”; thin black lines) vs 1.25% W_{10} (gray lines) over the time the LRPADS was deployed. The latter is a good “rule of thumb” estimate of the surface Stokes drift. The former is thought to be tightly related to the actual Stokes drift, although somewhat noisy. The overall correspondence between the two estimates is good. Note the antiphase oscillations at tidal frequencies in the two estimates of the eastward component on days 272 through 276 (yearday 274 = 1 October 2002). A negative eastward component corresponds to downwind flow, because the wind is from the east.

lution of bubble clouds are slow compared to the time needed to resolve advection (10–30 s), the feature-tracking result is an average of the Lagrangian velocity over both the observed surface area and the bubble depth distribution.

The Doppler estimates too are weighted in the vertical by the bubble cloud density; however, they may also be affected by the sheltering of wave crests, because acoustic rays must pass under the preceding wave troughs. For sound incident from below at angles steeper than the wave slopes, the measurement volume rises and falls with the bubble clouds, but has fixed range bounds. Thus, without sheltering the Doppler measurement volume moves vertically but not horizontally. As noted in section 2, one-half of the Stokes drift comes from vertical displacements, and one-half from horizontal, so in this case the difference between FDVs should correspond to one-half of the Stokes drift [because the former includes it in full and the latter only by half, as noted by Smith (1992)]. In contrast, at grazing angles wave troughs shelter more distant wave crests, limiting the measurement volume to a more nearly fixed depth interval below the typical wave trough depth. This leads to an expected difference between the previously reported 1990 versus 1995 results. With a typical wave steepness of 0.1 and a sonar deployment at 35-m depth, as in the 1990 deployment (Smith 1992), the former behavior would be expected out to an about 350-m range, which is nearly full range in that case. With a sonar deployment at 15-m depth, as in the 1995 deployment (Smith 1998), some sheltering of crests is expected beyond 150 m; focusing on ranges from 200 to 450 m, sheltering is expected there, and the result comes closer to the full Stokes drift.

To develop a model of the Doppler response, consider the depth weighting resulting from bubbles. In the ocean, bubble density generally decreases exponentially below the surface, with a depth scale (depending weakly on wind speed) of the order of 1.5 m for 10 m s⁻¹ winds (Thorpe 1986; Crawford and Farmer 1987). A reasonable model for the bubble distribution is

$$B \approx B(x, y, t)e^{k_b z}, \tag{4.1}$$

where $B(x, y, t)$ can vary over several orders of magnitude (Crawford and Farmer 1987), but the depth scale $k_b \approx (1.5 \text{ m})^{-1}$ is assumed not to vary significantly in time or space. The bubble-weighted depth average of a quantity “ $q(z)$ ” is formed from some upper limit z_s downward, where the “sheltered depth” z_s may be below the actual surface because of sheltering (discussed further below),

$$\bar{q}^z = \frac{\int_{-\infty}^{z_s} qe^{k_b z} dz}{\int_{-\infty}^{z_s} e^{k_b z} dz} = k_b e^{-k_b z_s} \int_{-\infty}^{z_s} qe^{k_b z} dz. \tag{4.2}$$

A surface wave of frequency f and corresponding wavenumber k_f yields a response of the form

$$\begin{aligned} u_m(r, t) &= \overline{u(r, t)^z} \\ &= U_0 \cos(\theta_k - \theta_r) e^{i(k_r r - 2\pi f t)} \frac{k_b e^{k_f z_s}}{k_b + k_f} \\ &= u_r(r, t) \left(\frac{e^{k_f z_s}}{1 + k_f/k_b} \right), \end{aligned} \tag{4.3}$$

where the nominal radial current u_r is defined at the mean surface, $z = 0$. The final response factor in (4.3) can be used to adjust the measured velocities to estimate what the value would be at $z = 0$ or $z = \zeta$. Near the high- k cutoff ($k_f \approx 0.39 \text{ rad m}^{-1}$), the denominator is about 1.6. The denominator is a fixed correction (i.e., independent of z_s) that can be performed simply in the frequency domain using linear dispersion to get k_f . This correction is henceforth taken as applied, and the term is dropped from explicit analysis. The remainder of the effect lies in the placement of the upper limit of the average z_s . For a wave of wavenumber k_f , the result can be adjusted to the semi-Lagrangian surface velocity U_ζ and Eulerian velocity U_0 (see Fig. 4),

$$\begin{aligned} U_\zeta(r, t) &= u_m(r, t)e^{k_f(\zeta - z_s)} \quad \text{and} \\ U_0(r, t) &= u_m(r, t)e^{k_f(z_0 - z_s)}, \end{aligned} \tag{4.4}$$

where z_0 is a chosen fixed depth (e.g., a typical wave trough depth). Each wave component has a different depth scale k , while the sheltered depths $z_s(r, t)$ and elevations $\zeta(r, t)$ are defined in the time–space domain from the entire ensemble of waves. Thus, applying this adjustment to the data requires the equivalent of a “slow” Fourier transform. This is discussed further in section 5.

To examine the effects of acoustic sheltering of wave crests, and the transition between the two limiting behaviors, simulations were performed. Effects of the sheltering on both wave orbital velocities and on a background surface shear layer are considered. Sheltering is determined by a simple algorithm, considering a single sonar beam in isolation, and by assuming the acoustic rays are straight (although the bubbles affect sound speed and hence cause refraction, the distances from troughs to crests are too short for the rays to refract significantly, so this approximation is reason-

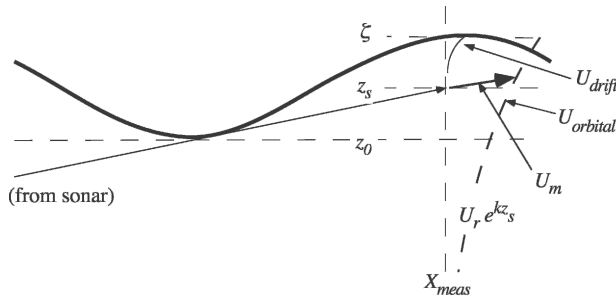


FIG. 4. Schematic of sheltering geometry, showing the upper bound of the measurement volume “ z_s ” and the nominal depth dependencies of a wave and the drift current profiles.

able). First, a wave elevation profile $\zeta(r, t)$ is defined as a function of range and time, in a form similar to that of the velocity data. Then, the array of vertical angles from the sonar to the center of each range bin is defined via its sine, which is the ratio of $\zeta +$ sonar depth to the radial distance. Starting from zero range and working outward, the minimum value of all previous sine angles out to the target range is retained (Fig. 5). Applying the results of (4.3) or (4.4) (see Fig. 4 again), mean velocities calculated at the moving surface, at a fixed level (near a typical trough depth, say), and at the simulated sheltered depths in between can be directly compared (Fig. 6). The sheltered depth always lies between the actual surface and the depth of the wave troughs; thus, the result lies between a surface-tracking semi-Lagrangian estimate and a Eulerian estimate at the depth of a typical wave trough. The simulations show how measured values should differ from surface-following versus fixed-depth values as a function of range: the Doppler measurement (dotted line, Fig. 6) matches the surface-tracking value (dashed line, Fig. 6) over the first 150 m, and then moves gradually toward the fixed-depth value (x axis, Fig. 6) at the most distant ranges, as anticipated. The transition is not quick. For

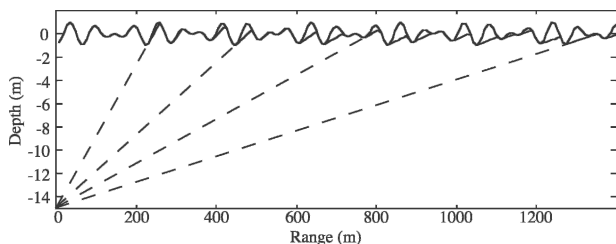


FIG. 5. Schematic of acoustic sheltering of wave crests vs range. The simulated surface elevation (solid black line); sheltered depths or upper limit of acoustic probing z_s (solid gray line); and some of the acoustic paths from the sonar, starting at 15-m depth (dashed lines). For typical wave conditions, sheltering does not occur before 150–200-m range.

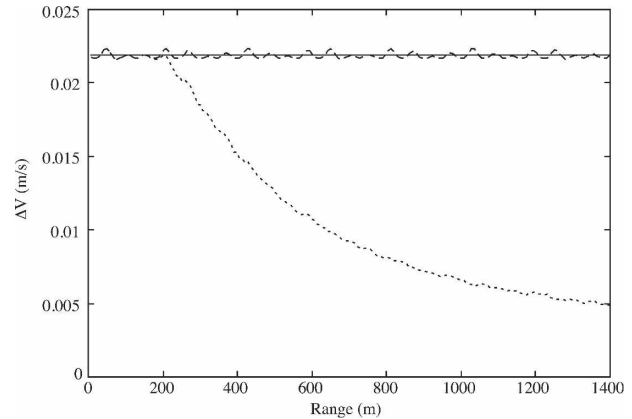


FIG. 6. Time-mean velocity differences in the simulated data. Synthetic measured velocity minus the Eulerian reference, $U_m - U_0$ (dotted line); surface velocity minus Eulerian, $U_\zeta - U_0$ (dashed line); the theoretical $\langle U_\zeta - U_0 \rangle$ for the input spectral lines (solid line). The synthetic measured velocity is at the calculated sheltered depth z_s ; the Eulerian velocity is at fixed depth $z_0 = -\text{RMS}(\zeta)$; the semi-Lagrangian velocity is at the surface ($z = \zeta$), but not displaced horizontally. The solid and dashed lines should both correspond to one-half of the Stokes drift.

the wave steepness and sonar depth as simulated, the transition is only 50% complete at 600-m range. Using estimates averaged over a middle segment (say 300–1200 m), the difference between the Doppler mean and feature-tracking velocities is expected to be about 75% of the Stokes drift. Because wave steepness is robust, the calibration coefficient between the FDV and true Stokes drift should remain roughly constant for a given deployment geometry.

The presence of a thin wind-drift layer also affects the sheltering results. For simplicity, consider a steady wind-drift layer with an exponential drift profile with scale depth k_d^{-1} . As described in Smith (1986), the overall character of the wind-drift layer is well captured by this approximate form, and the results are easily manipulated and understood. The drift layer is assumed to move up and down with the free surface. Modulation of the wind drift by the waves is neglected, because this is expected to be small except very near breaking (Longuet-Higgins 1969a; Banner and Phillips 1974; Smith 1986). Then, the weighted-average response (4.3) applies, with k_d substituted for k_f . Given the wind-drift strength and depth scale, the effect on measured velocities can be efficiently estimated as

$$u_m^d(r, t) = u_d \left[\frac{e^{k_d(z_s - \zeta)}}{1 + k_d/k_b} \right]. \quad (4.5)$$

A reasonable estimate of the surface wind drift u_d is 1.6% W_{10} , where W_{10} is the wind speed at 10-m height (Wu 1975; Plant and Wright 1980). With just molecular

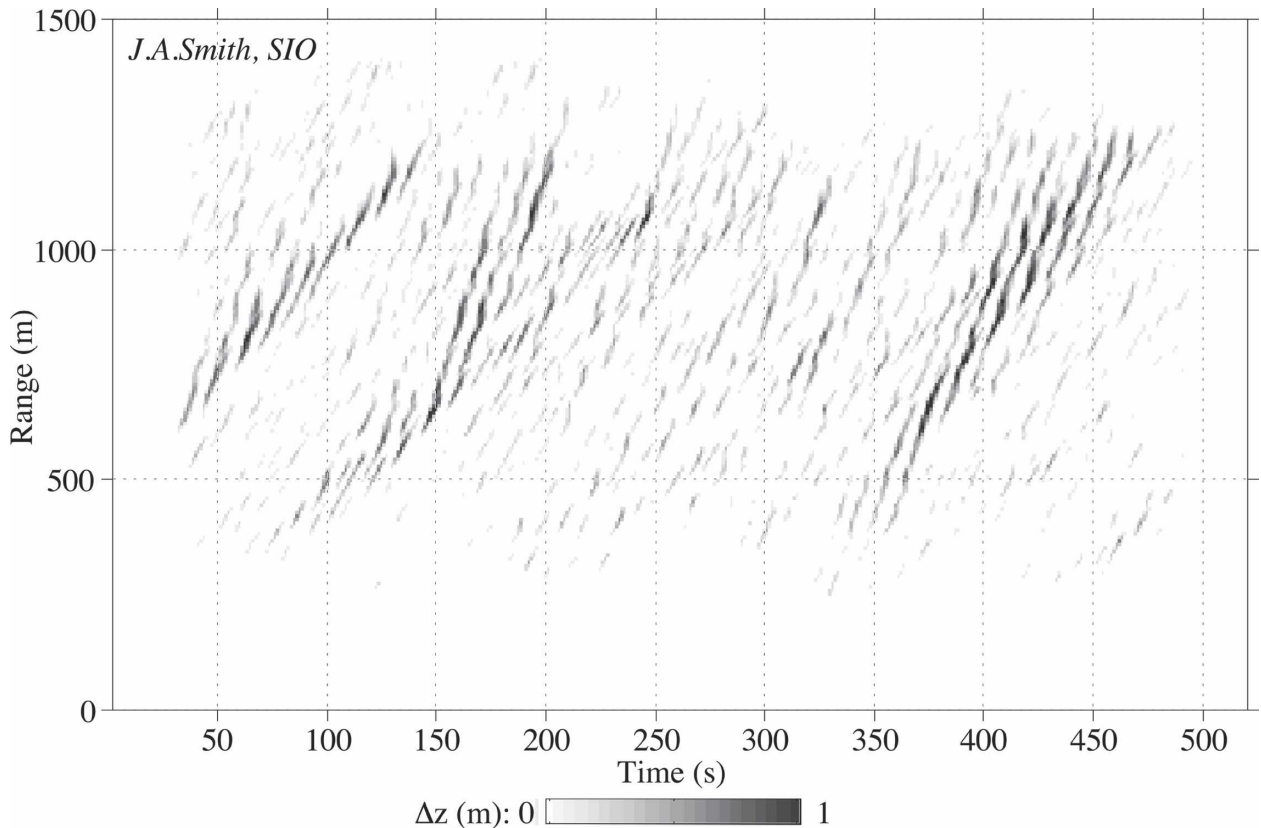


FIG. 7. The sheltering thickness (depth of upper-acoustic sampling limit below the actual surface; values are positive only) estimated from field data. Elevation is estimated from radial velocity [see section 5, (5.14); corresponding velocity data are shown in Fig. 9], then the acoustic shading algorithm is applied. Waves propagating at right angles to the beam are ineffective at sheltering, so loss of sensitivity to such waves because of sensing only the radial component is unimportant in this calculation. The estimated deficit in wind drift resulting from sheltering looks very similar (but with a scale change from 1 m to about 15 cm s⁻¹).

viscosity, the drift layer would be just millimeters thick, and this average would be negligible. Following Smith (1983), a “law of the wall” style turbulent drift layer with $z_0 \approx 0.004$ cm (as observed in the atmosphere in similar conditions) would still result in a layer only about 2.4 cm thick, for which the denominator of 4.5 is still over 60. However, breaking waves have a significant influence on the near-surface turbulent shear structure. A wave-induced eddy viscosity as described by Terray et al. (1996) would result in a wind-drift depth scale comparable to the rms wave amplitude. In simulations, the greatest effect from drift sheltering occurs for wind-drift depth scales between the sheltering thickness and the bubble depth scale. The rms wave amplitude is in this range, so its use yields a roughly maximal estimate of the drift-layer effect. From simulations, the two main effects are 1) a slight decrease in the mean downwind flow in proportion to sheltering, and 2) a decrease in the measured orbital velocities with increased sheltering, because the forward velocity in each crest is decreased by the amount of missing

wind drift there. The former produces an increase in the predicted FDV, because the missing drift only affects the Doppler measurement and so helps explain the tendency toward the full value of Stokes drift found in the observations; that is, the missing drift partially compensates for the missing Stokes drift. The latter helps explain a systematic decrease in wave amplitude with range, although finite angular spreading of the beams has a similar effect resulting from the crossbeam smoothing of wave motion. Other effects of clipping the wind-drift layer, which appear at wave harmonics and at group envelope scales, are smaller and can be neglected.

Sheltering can be estimated for the actual data using this same algorithm (Fig. 7). The method for estimating elevation from time–range segments of radial velocity is outlined in section 5. In the data segment shown here, the sheltering thickness increases to 0.5–1 m at the greatest ranges, which is only slightly smaller than k_b^{-1} . For the wind-drift parameters used here (1-m depth scale, 16 cm s⁻¹ surface value), estimated drift anoma-

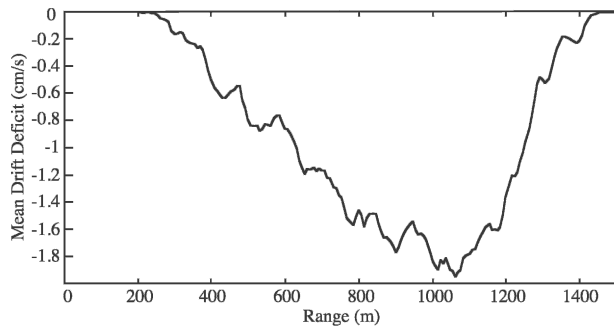


FIG. 8. The time-mean reduction in measured surface drift because of sheltering, for a wind drift with 1-m depth scale and surface magnitude 16 cm s^{-1} . This effect contributes to the difference between the feature-track- and Doppler-derived means (FDV), increasing it from 75% to roughly 92% of the estimated value of Stokes drift.

lies are roughly proportional to the sheltering thickness, with maxima near 15 cm s^{-1} (this would look like Fig. 7, but with $0\text{--}15 \text{ cm s}^{-1}$ amplitude scale). Figure 8 shows the time-mean drift anomaly from the same data (and wind-drift magnitude and depth scale). Assuming an area mean can be substituted for a time mean (and vice versa), this would correspond to an increased FDV estimate as well. Because the wind-drift deficit amounts to about $1/6$ of the Stokes drift in magnitude, this would bring the FDV value (formed over 200–1100 m in range) up from 75% to about 92% of the Stokes drift. Last, the estimated leakage into group envelope characteristics and into higher harmonics of the waves is small, as anticipated from the simulations. This ordering of effects is corroborated by the backscatter intensity data, which act mathematically like a proxy for a wind-drift layer (though perhaps with a different depth scale); as the exponentially surface-trapped bubbles are moved up and down into sheltered regions, the resulting modulation of the intensity signal is strong along the surface wave dispersion part of the corresponding k - f spectrum, but undetectable along the 5 m s^{-1} propagation line corresponding to group envelope characteristics.

The explicit extrapolation of wave motion from sheltered depths to both the moving surface and a fixed level provides an alternative way to evaluate the Stokes drift: the difference between the two is half of the drift. In addition, this approach provides objective estimates of the Eulerian velocity fields. This is developed below (section 5) as method 3.

5. Stokes drift estimates using frequency-wavenumber spectra

In this section, estimation of time-space maps of the radial component of Stokes drift along a given sonar

beam direction is considered. The objective is to produce estimates of the Stokes drift that are directly analogous to the radial velocity measurements of the underlying flow for each beam. Then, time-range propagation characteristics of the Stokes drift can be examined to see 1) how intermittent the wave influence or interaction might be, and 2) how it compares with the observed underlying flow. Two methods are developed, using frequency-wavenumber Fourier coefficients formed from time-range data slices.

A natural and useful slice through the 3D time-space data volume is a time-range plot, formed along a single direction. Because the heading of *FLIP*, and hence of the array, can vary by tens of degrees over time scales of minutes, the beam-formed data are first interpolated onto a set of fixed directions. Time-range plots reveal both phase propagation and group (envelope) characteristics of surface waves along a given direction. For example, Fig. 9 shows a time-range plot for a beam directed roughly downwind. Compact packets of roughly 7-s-period waves can be seen, forming slashes at an angle on the time-range plane corresponding to about 5 m s^{-1} (the group velocity for 7-s waves, which also have a phase velocity near the wind speed, 10 m s^{-1}). These compact packets are distinct from the spectral peak waves (near 10.6 s), which form broader groups (e.g., in Fig. 9 note a longer group starting at 300 s and propagating upward at a steeper angle, near 7.5 m s^{-1} , reaching 1000 m at about 435 s).

Figure 10 shows the log magnitude of the 2D Fourier transform of the velocity data shown in Fig. 9, color contoured on the k - f plane. Because the data are real, the $(+f, +k_r)$ components are redundant with respect to the conjugate $(-f, -k_r)$ components. The wavenumbers are shifted so that $k_r = 0$ is centered. The frequencies are not shifted, so the variance for frequencies past the Nyquist frequency, which are aliased onto negative frequencies, aligns with the unaliased variance along the surface wave dispersion curve. The continuity of variance along the dispersion curve suggests this aliased information can be used. Because of the external knowledge that the waves propagate predominantly downwind, the ambiguity of location on the aliased k - f plane is resolved. As seen in Fig. 10, the resolved (but aliased) surface wave variance extends well past the frequency Nyquist limit, $f_N = 0.2 \text{ Hz}$, to more than 0.3 Hz . After masking (zero filling) to remove redundant information, the remaining k - f Fourier coefficients are interpreted with the convention of time going forward and waves propagating in the same direction as \mathbf{k} ; that is, the $(+f, \pm k_r)$ half-plane is retained, and the amplitudes are adjusted to preserve the net variance.

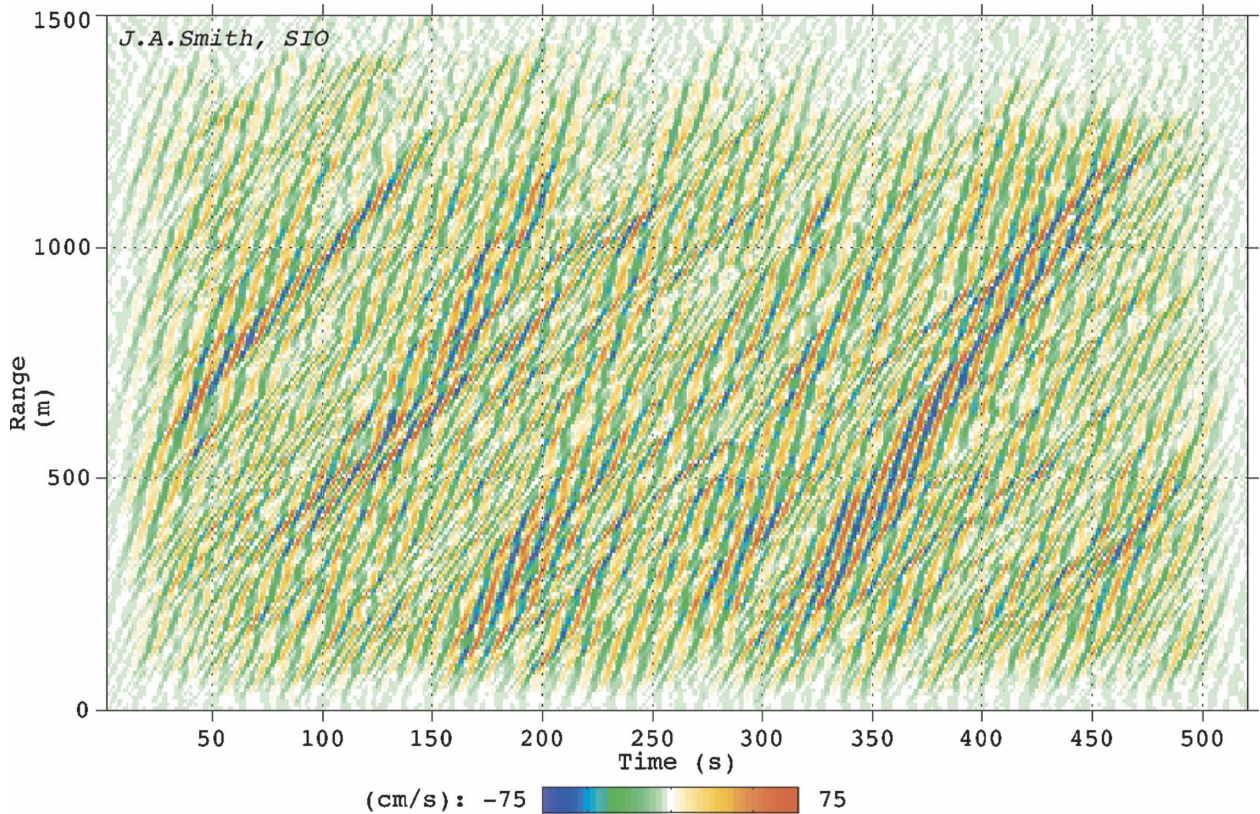


FIG. 9. Time–range plot of radial velocities, dominated by the surface wave orbital velocity. The spectral peak is near 0.1 Hz; note a large wave group starting near 0-m range at 300 s, and moving out to 1000-m range by 435 s, corresponding to a group velocity of about 7.5 m s^{-1} . Several thinner “slashes” are seen propagating a little slower, at a speed of about 5 m s^{-1} . These slashes are compact wave groups of order one wavelength long (along the vertical axis; i.e., spatially). The frequency associated with these compact groups is near 0.14 Hz (7-s period). The group speed is about 5 m s^{-1} , and the corresponding phase speed is about equal to the wind speed, 10 m s^{-1} .

To resolve the unwrapped wave information, the FFT size is doubled in the f direction. The inverse Fourier transform thus has results interpolated to twice the sample rate (samples every 1.25 s rather than 2.5 s).

The original processing used the nominal range resolution for this data of 10.6 m. The downwind surface wave dispersion branch was seen to extend beyond the corresponding Nyquist wavenumber $k_N = 0.047 \text{ cycles m}^{-1}$, wrapping a second time into the low-frequency, low-wavenumber region. Resolving this double alias was important not only for effectively enhancing the resolution of the surface wave measurements, but also because this second alias of the wave variance would otherwise be falsely identified as being slower-moving “nonwave” activity. Retaining the raw data made it possible to resample at 7.5-m resolution in range, resolving this problem. While the error variance of each estimate is increased, the increase is in proportion to the increase in area on the k axis; that is, the spectral noise floor remains the same.

a. Linear dispersion and spectral bounds

The k – f spectra strongly favor waves propagating directly along the beam. This is largely because of the cosine response of the measured along-beam velocity component to propagating waves. On the k – f plane, the linear dispersion curve is $k_r \approx k_f$, where k_f is the magnitude of the wavenumber for a given frequency f . In deep water, and including advection by a mean velocity U , linear dispersion yields (note conversion from Hz to rad s^{-1})

$$\sigma = 2\pi f = (gk_f)^{1/2} + Uk_f \cos(\theta_k - \theta_u), \quad (5.1)$$

where $\theta_k - \theta_u$ is the angle between the wavenumber and the mean flow directions. This can be inverted into a form that is stable with respect to $U \rightarrow 0$ (substitute $x = k_f^{-1/2}$),

$$k_f = \left[\frac{2\sigma g^{-1/2}}{1 + [1 + 4U\sigma g^{-1} \cos(\theta_k - \theta_u)]^{1/2}} \right]^2 \quad (5.2)$$

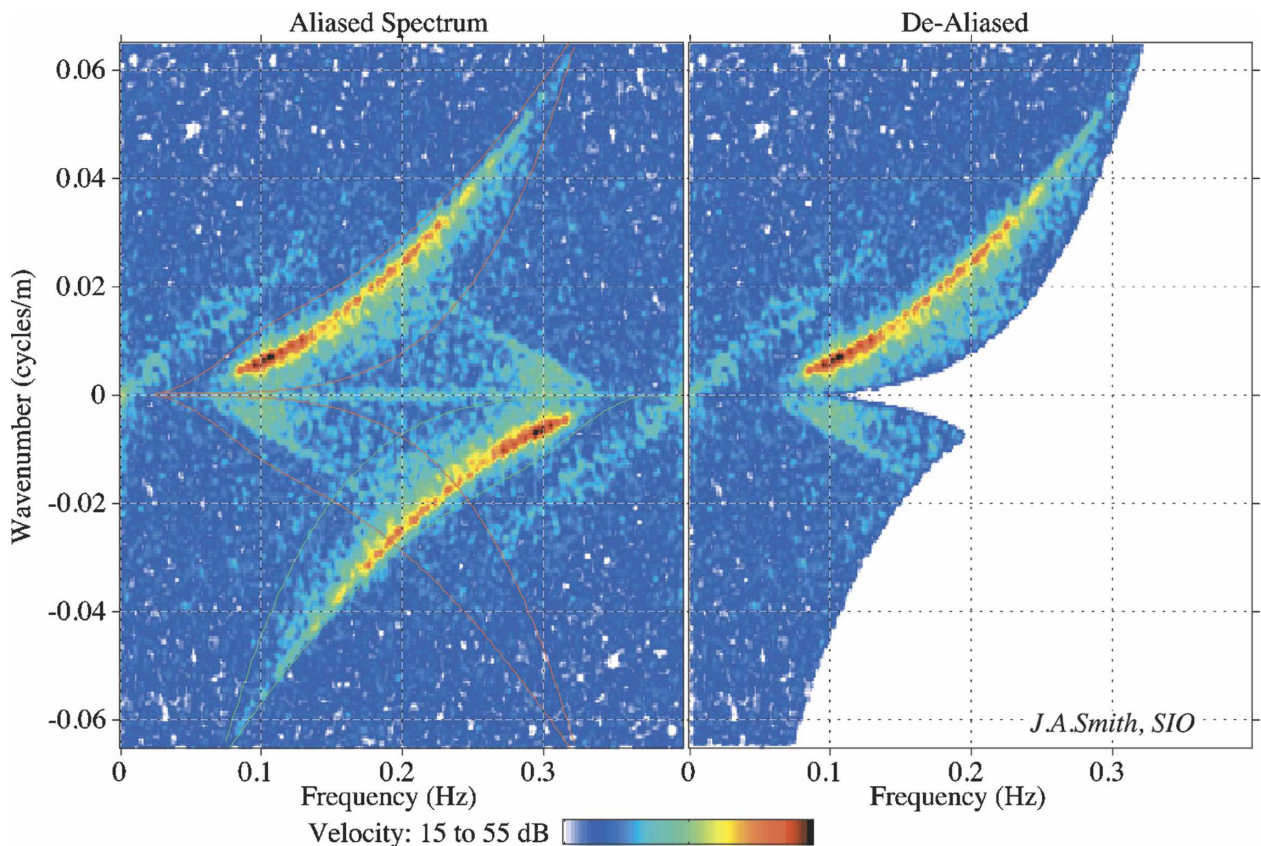


FIG. 10. Wavenumber–frequency spectrum from the data shown in Fig. 9. (left) Full spectrum with aliased content; (right) spectrum with aliased data and some of the noise near $k = 0$ masked off. In addition to surface wave variance (outlined in red on the left), a weaker ridge of variance lies along a line at roughly 45° , corresponding to propagation at about 5 m s^{-1} . This variance is broadly distributed in k and f , so it would be difficult to isolate without both the k and f information. The red lines are also used to delimit the separation between “wavelike” from “nonwave” variance in the spectral domain.

[Smith and Bullard 1995, their (4.2); however, note that their (4.1) is erroneous]. At higher wavenumbers advection becomes more noticeable on two counts: first, the fractional change in k at fixed f and U is larger because of the decreasing phase speed (so $U\sigma g^{-1}$ is larger); and second, for a larger value of k the spectral resolution is a smaller fraction of k . Thus, at the high-wavenumber end resolved here (near-3-s period) velocities of even a few centimeters per second make a detectable difference. Note also that the advection velocity of the shorter waves includes the Stokes drift of the longer waves; at the level of accuracy required here, this can be parameterized as 1.25% W_{10} (wind at 10-m height), which is added to the Doppler mean estimate.

Surface waves are both the fastest-moving and the largest-amplitude signal detected. To delimit the area on the k – f plane dominated by waves, objective bounds on k_r versus f are determined based on a balance between wave variance and the noise floor of the measurement. Dimensional analysis, assuming all but grav-

ity to be small influences, yields an “equilibrium spectrum” for surface orbital velocity variance of the form

$$P_u^2(f) \propto f^{-1}(g/f)^2 \propto f^{-3}. \quad (5.3)$$

On the k – f plane this variance is spread out from $k_r = 0$ to $k_r = k_f \propto f^2$, so that

$$\begin{aligned} P_u^2(f, k) &\propto f^{-5}, \\ -k_f < k_r < +k_f. \end{aligned} \quad (5.4)$$

The cosine response of the radial current measurement results in a further k_r dependence, yielding

$$P_u^2(f, k_r) = P_u^2(f) k_f^{-1} \cos^2(\theta_k - \theta_r) \propto f^{-5} (k_r/k_f)^2 \propto f^{-9} k_r^2. \quad (5.5)$$

Thus, the bound is set according to

$$k_{\text{low}} \equiv k_r(\text{lowerbound}) \propto f^{-4.5}. \quad (5.6)$$

To set the constant for this limit, the curve is made to intersect the linear dispersion curve where the latter

fades into the noise. For example, in Fig. 10, $k_{\text{low}} = k_f$ is enforced at $k_{\text{tr}} = 0.065$ cycles m^{-1} , with the corresponding frequency $f_{\text{tr}} \approx 0.33$ Hz.

The upper bound must be above the dispersion curve because of finite spectral leakage. The upper limit is not as critical as the lower because 1) the variance there is primarily spectral leakage, and 2) adjustments to be applied that involve dividing by $\cos(\theta_k - \theta_r)$, for example (see below), are not singular there. Here the upper limit is set assuming (typical) spectral leakage of the form

$$P(k_f + \delta) \propto f(\delta) \rightarrow \delta^{-n}, \tag{5.7}$$

where the limit is approached quickly; that is, for δ more than a few times the spectral resolution Δk . To form a simple parametric curve describing the total energy at f , we assume that P_u^2 approaches an f^{-3} decay at high frequency (as before), is maximal at some specified frequency f_0 , and rolls off to zero for small f even faster, say, as f^6 . Allowing for leakage behavior as in 5.7 with $n = 2$, and adding this to dispersion, a curve of the form

$$k_{\text{hi}} = k_f + \frac{2D_0}{(f/f_0)^{3/2} + (f/f_0)^{-3}} \tag{5.8}$$

is adopted, where D_0 is a specified maximal distance above the dispersion curve, achieved at $f = f_0$. For example, in Fig. 10, the values $D_0 = 12(\Delta k)$ and $f_0 = 0.1$ Hz were used, where Δk is the spectral resolution for the finite FFT employed (≈ 1 cycle per 2.7 km). Last, a small amount (Δk) is subtracted to permit more low-frequency/low-wavenumber variance to pass, because surface waves longer than 30 s or so are not seen in this dataset, and some of the “5 m s^{-1} variance” crosses the axis at small but finite frequencies.

b. Stokes drift from LRPADS radial velocity data

Estimation of the radial (along beam) component of Stokes drift along individual beams of the LRPADS data is now addressed. Waves propagating at right angles to the beam contribute nothing to the net along-beam drift, so it is unimportant that the measurements from the beam are insensitive to such waves. The results from all of the beams can be combined so the full space–time evolution of the Stokes drift can be evaluated, and time–space maps of the radial Stokes drift can be directly compared to the underlying nonwave flow measured simultaneously.

The two methods developed here work from the 2D k – f Fourier coefficients. Zero padding the negative frequencies and doing the inverse transform results in both the (oversampled) original time series (real part of

the result) and a constructed out-of-phase part (or Hilbert transform; imaginary part). For a narrowband process, the absolute value corresponds to the envelope of the radial component of velocity

$$|u_r(r, t)|^2 = |u|^2 \cos^2(\theta_k - \theta_r), \tag{5.9}$$

whereas the radial component of Stokes drift

$$u_r^S(r, t) = u^S(r, t) \cos(\theta_k - \theta_r) = c^{-1} |u|^2 \cos(\theta_k - \theta_r) \tag{5.10}$$

is the quantity of interest. The phase speed c is a simple function of frequency: from dispersion

$$c \equiv \sigma/k_f = 2\pi f/k_f. \tag{5.11}$$

To reduce from $\cos^2\theta$ to $\cos \theta$ requires dividing by (k_r/k_f) , which is singular at $k_r = 0$. The objectively derived low- k cutoff (5.6) provides the necessary tool. Rather than truncate sharply at k_{low} , an arbitrary but smoothly weighted function is employed of the form

$$W(k_r, f) = \left(\frac{x^3}{1 + x^4} \right) \left(\frac{k_f}{k_{\text{low}}} \right), \quad \text{where} \tag{5.12}$$

$$x \equiv \frac{k_r}{k_{\text{low}}(f)}$$

and k_{low} is defined in (5.6). This has the desirable properties that it 1) $\rightarrow 0$ rapidly as $k_r \rightarrow 0$; 2) $\rightarrow [\cos(\theta_k - \theta_r)]^{-1}$ rapidly for $k_r > k_{\text{low}}$; 3) decreases smoothly through the threshold value $k_r = k_{\text{low}}$; and 4) retains the sign of k_r .

One way to obtain estimates of the Stokes drift is to weight the Fourier coefficients by the square root of the net conversion factor,

$$P_u(k_r, f) \rightarrow P_u(k_r, f) [W(k_r, f)/c(f)]^{1/2}. \tag{5.13}$$

This, when reverse transformed, yields a “root velocity” field whose absolute value squared is (nominally) the Stokes drift (this is “method 2”). However, note that the sign of k_r is important: the Stokes velocity from incoming waves is in the opposite direction from those that are outgoing. The weighting function W also changes sign, but here this yields an imaginary factor, which merely alters the phase of the “carrier wave.” Because the transforms are complex and absolute values are eventually taken, the change in sign is ignored. The simplest fix is to treat the $+k_r$ and $-k_r$ parts separately. Here the upwind-directed portion is so weak that only the downwind portion needs to be treated. Method 2 has the advantage of speed, because it employs only FFT operations and a weighting; yet it provides more detailed time–space information than method 1, the area-mean FDV.

Another approach is to take advantage of the fact that for deep-water waves the vertical displacements alone can be used to estimate one-half of the difference between the Lagrangian and Eulerian velocities (method 3, as indicated in sections 2 and 4). To this end, the velocity fields are extrapolated vertically from the measurement level to both a constant level (e.g., $z = 0$) and to the moving surface (at $z = \zeta$). Method 3 has the advantages of (a) explicitly considering the sheltering of crests, (b) properly handling upwind- versus downwind-directed components, and (c) providing objective estimates of the Eulerian and semi-Lagrangian flows, corrected for sheltering effects.

Elevation displacements ζ are needed to evaluate sheltering and also to implement method 3. These are to be estimated from the radial component of horizontal velocity, which is insensitive to waves propagating at right angles to the beam. To control singularities in this estimate, we use

$$\zeta = \left[\frac{\sigma^{-1} u_r}{\cos(\theta_k - \theta_r)} \right] \approx \sigma^{-1} u_r W(k_r, \sigma), \quad (5.14)$$

where W is the inverse-cosine weighting function with a built-in cutoff defined above (5.12). Because both the radial Stokes drift and the sheltering effects are also insensitive to the perpendicularly propagating waves, the loss of information about them is ultimately not important.

The estimated elevations are used to explicitly calculate displaced and fixed-level radial velocities, frequency by frequency:

$$u_r^\zeta(r, t, f) \approx [P_u(r, f) e^{-i(2\pi f)t}] e^{k_f(\zeta - z_s)}, \quad (5.15)$$

and

$$u_r^0(r, t, f) \approx [P_u(r, f) e^{-i(2\pi f)t}] e^{-k_f z_s}, \quad (5.16)$$

where z_s is the sheltered depth discussed in section 4, both z_s and ζ are functions of range and time, and the subscript r denotes the radial (along beam) component of velocity. Note that the total displacement fields $z_s(r, t)$ and $\zeta(r, t)$ are used for all frequencies; this makes the method 3 result fundamentally different from that of method 2. The portion inside the brackets is understood as an inverse Fourier operation carried out on a single frequency component (there may be an additional normalization factor, depending on the Fourier transform definition used). The results are integrated over f at each location in range–time space (or, for discretely sampled finite-length data, summed) to yield the net displaced (semi-Lagrangian) and fixed-level (Eulerian) radial component of the velocity fields. The wave-averaged difference between the vertically dis-

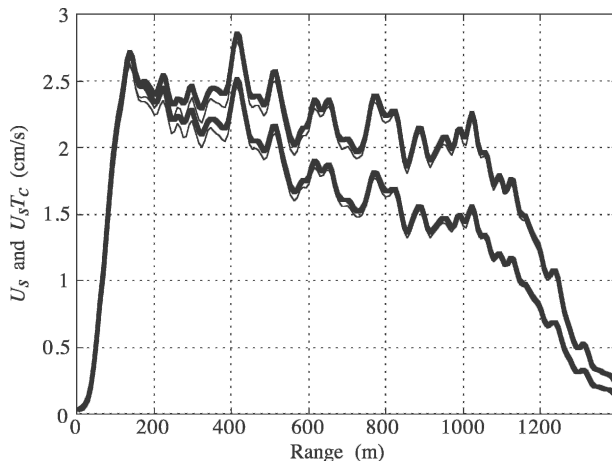


FIG. 11. Mean estimated radial component of Stokes drift U_s for the same time and beam as shown in Fig. 9: (bottom) U_s from twice the difference between U_ζ and U_0 [thick line; (5.17)], and U_s from the magnitude squared of adjusted spectral coefficients [lower thin line; (5.13)]. (top) Same, respectively, but adjusted by a linear increase with range (see section 6).

placed and fixed-level velocities is one-half of the Stokes drift, so the estimate by method 3 is

$$u_r^S(r, t) \approx 2\langle u_r^\zeta - u_r^0 \rangle, \quad (5.17)$$

where $\langle \rangle$ denotes an average over the waves. Here the k - f plane separation described above is used to separate wavelike and nonwave variance. Note in particular that the 5 m s^{-1} ridge extends far enough in both f and k that a simple time filter alone would be insufficient to separate it from the waves. Extensive combined space and time information is required to detect this phenomenon.

Results of the root velocity [(5.13)] versus the displacement [(5.17)] methods (2 and 3) for estimating the Stokes drift are close but not identical. Figure 11 shows a comparison between the time-mean Stokes drift estimates via the two methods versus range over the same data segment as shown in Fig. 9. The agreement is good, verifying that the upwind-directed waves are negligible and that the narrowband assumption is a weak requirement. Both methods lead to Stokes drift estimates that weaken with range. The estimated effect of a nominal wind-drift layer (see section 4) was incorporated, which also helps to flatten this response profile slightly, but lateral averaging remains as the beams spread. The range resolution of 7.5 m matches the beamwidth near 330-m range. Beyond this range the crossbeam smoothing dominates, and waves at any finite angle to the beam experience progressively more suppression. Estimates adjusted by a linear increase with range is also shown; this increase is statistically related to the ob-

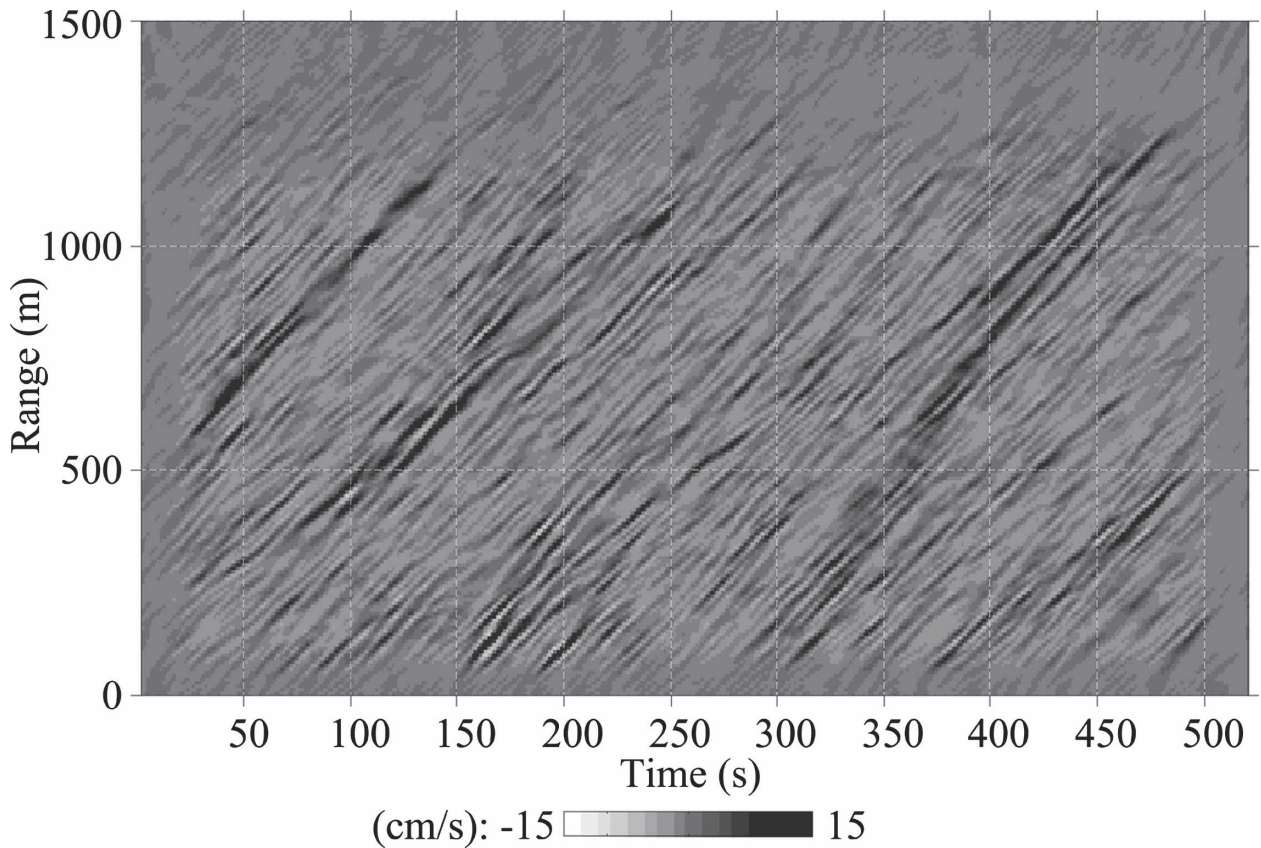


FIG. 12. Time–range plot of the radial Stokes drift for the same data segment as in Fig. 9 (time means at each range are removed; see Fig. 11). Note the predominance of darker “slashes” at an angle corresponding to roughly 5 m s^{-1} propagation along the beam. Comparing this with Fig. 9, it can be seen that the high Stokes drift events are largely associated with the smaller-scale but intense “packets” of 7-s waves, while weaker activity results from the larger-scale 10-s waves.

served Eulerian response, and is discussed in section 6 below.

Figure 12 shows a time–range plot of the radial Stokes drift for the same time segment and beam as in Fig. 9, using the displacement method (5.17). The results clearly show wave groups, as expected. Note particularly the correspondence between the strongest Stokes drift signals and the compact higher-frequency groups propagating at roughly 5 m s^{-1} seen in Fig. 9.

For a spectrum of the form posited above, the net contribution to Stokes drift drops off weakly as a function of frequency,

$$u^S(f) \approx P_u^2(f)(2\pi f/g) \propto f^{-2}. \quad (5.18)$$

The high-frequency tail of the spectrum affects the Stokes drift at the actual surface. This can be addressed by parameterization in terms of a local equilibrium with the wind (e.g., as in Hara and Belcher 2002), or by using higher-frequency unidirectional data (e.g., from an elevation resistance wire) combined with an assumption that the high-frequency waves propagate downwind

with some approximately known directional spread. However, in the context of the forcing of LC or the evolution of bubble clouds, an average over some small but finite depth (say, that of the bubble clouds) is more dynamically relevant. An exponential average of the Stokes drift over $k_b \approx (1.5 \text{ m})^{-1}$ results in an effective spectral cutoff near $k_f = k_b/2 \approx (3 \text{ m})^{-1}$ (in radians), corresponding to a linear wave of $f \approx 0.3 \text{ Hz}$ frequency. For example, Kenyon’s (1969) solution applied with the equilibrium spectrum of Pierson and Moskowitz (1964) yields a surface value of about 4% W_{10} , but a bubble-weighted average of about 1.2%, which is remarkably close to the 1.25% value quoted above. Thus, it appears (coincidentally) that the enhanced effective resolution of the dealiased spectra is adequate to resolve the important part of the wave spectrum and hence of the resulting Stokes drift.

6. Observed response to wave groups

The next most prominent feature after the surface waves in the k – f spectra of velocity is a roughly linear

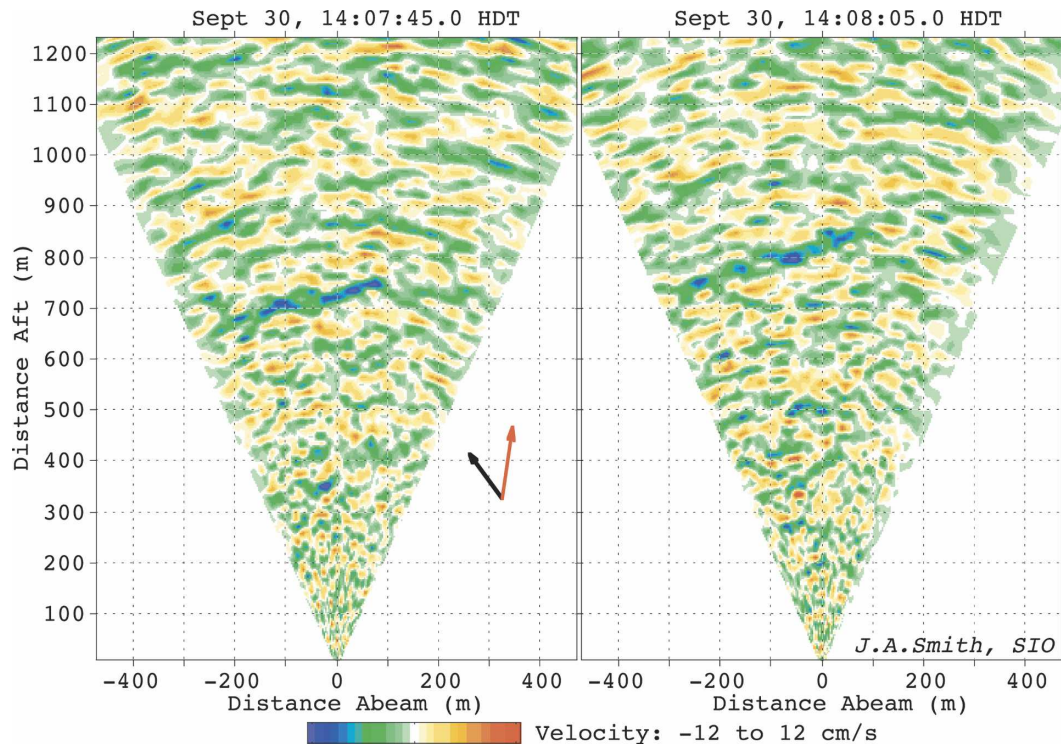


FIG. 13. Spatial distribution of radial velocity associated with the ridge of variance along the 5 m s^{-1} line in the k - f spectra. A spectral filter passing variance moving between 4.5 and 6.5 m s^{-1} (in either direction along each beam) was applied. The background “speckle” of $\pm 3 \text{ cm s}^{-1}$ or so is the noise level of the measurement as filtered. The darker blue band seen near 700-m range on the left and near 800 m on the right is the motion associated with the 5 m s^{-1} spectral ridge. The two frames shown are 20 s apart. The black arrow indicates the wind direction and speed ($\sim 10 \text{ m s}^{-1}$); the red arrow indicates the mean current ($\sim 15 \text{ cm s}^{-1}$). The feature is short in the along-wind direction, long in the crosswind direction, and moves at about 5 m s^{-1} .

ridge along a line near 45° (see Fig. 10), corresponding to about 5 m s^{-1} propagation speed. To see what form this activity takes in the time–space domain, a speed-based filter was applied in k - f space, passing variance moving between 4.5 and 6.5 m s^{-1} , which was then inverse transformed. Figure 13 shows two spatial images from the resulting sequence, 20 s apart (results from all beams, each processed independently). The features associated with this 5 m s^{-1} ridge are very narrow in the along-wind direction, but extend coherently a considerable distance in the crosswind direction. They consist of blue-shift anomalies (i.e., bands of upwind-directed velocity) that propagate downwind.

Figure 14 shows a time–range plot of the wave-filtered Eulerian velocity $U_0(r, t)$. The objective k - f bounds [(5.6) and (5.8)] shown in Fig. 10 were used to exclude the waves, and the results were inverse transformed back to time and range. Of particular note is that blue slashes in Fig. 14 resemble the dark slashes in the Stokes drift plot (Fig. 12). In fact, the sum of the two $U_0 + U_S$ yields a field of velocity that is nearly free of bias in propagation direction. This is verified most

clearly by comparison of the k - f spectra of the Eulerian (U_0) versus the net Lagrangian ($U_0 + U_S$) velocities (Fig. 15). The spectrum of the wave-filtered Lagrangian velocity has almost no hint of variance (other than noise) along the 5 m s^{-1} line, while the Eulerian-estimated field has a distinct ridge there. Note that the cancellation of Eulerian flow variance by the Stokes drift extends over a wide range of wavenumbers along this ridge. Inclusion versus exclusion of wind-drift sheltering effects (cf. section 4) had no discernable influence on these spectra.

The wave-filtered Eulerian velocity field is correlated with the Stokes drift at a statistically significant level (Fig. 16). With $N = 208$ samples (the number of pings over which the correlations are averaged), the coherence confidence level is (Thompson 1979)

$$C_\alpha^2 \approx 1 - \alpha^{1/(N-1)} = 1 - 0.05^{(1/207)} \approx (0.12)^2, \quad (6.1)$$

where α is the allowed probability of error ($\alpha = 0.05$ for 95% confidence). The correlation is several times larger than this level (0.3 – 0.4), so robust statistical es-

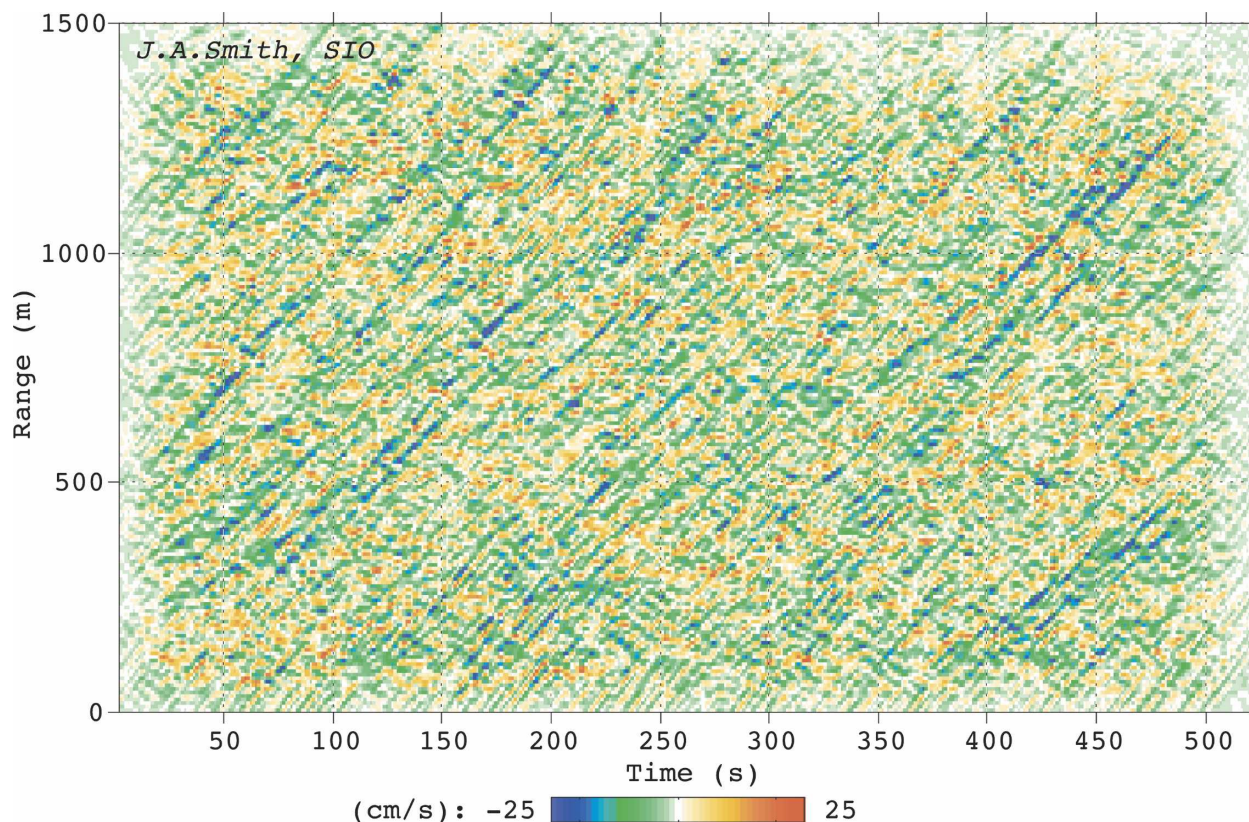


FIG. 14. Time–range plot of the wave-filtered radial Eulerian velocity U_0 along one beam. There is a predominance of blue slashes rising to the right, propagating at about 5 m s^{-1} . There is close resemblance between the blue slashes here and the dark slashes in the plot of Stokes drift (Fig. 12).

timates of the transfer function from Stokes drift to the Eulerian anomaly can be made,

$$T_c = -\langle U_S U_0 \rangle / \langle U_S^2 \rangle \quad (6.2)$$

(Fig. 17; note minus sign here). The Eulerian response is negatively correlated with the Stokes drift, with a transfer coefficient of about 1 and no spatial lag, indicating that the correlated parts cancel each other out. In fact, a slight increase of the estimated Stokes drift with range is needed to achieve complete cancellation everywhere. Given the azimuthal smoothing characteristics of the measurement, the underestimation of both the Stokes drift and the response is expected to increase with range. Because the Stokes drift estimates involve squared data while the response estimates do not, such smoothing has a larger effect on the former than the latter. A linear fit to T_c over the range interval of 200–1000 m is shown in Fig. 17. Interestingly, application of this as an “adjustment” to the Stokes drift estimates makes them vary less with range, without changing the near-range value (Fig. 11, upper curves).

The fact that the “ 5 m s^{-1} variance” disappears with

the transform to the estimated Lagrangian mean flow is convincing evidence that the Eulerian response is equal and opposite to the Stokes drift (in the near surface layer sampled). It is difficult to imagine any procedure that could lead coincidentally to such nearly perfect cancellation. Several other data segments have been examined (e.g., Fig. 13 is from a different segment than shown in Fig. 9); in each case such a cancellation of Stokes drift and Eulerian flow at the surface is observed.

7. Discussion: Wave groups and the expected response

Larger-scale motion forced by advancing groups of surface waves was discussed in some detail by Longuet-Higgins and Stewart (1962). While much of the interest centered on intermediate to shallow-water cases, the results have a sensible deep-water limit. To review the deep-water case briefly and simply, Garrett’s (1976) formulation is used, in which the wave effects appear as a “wave force” in the momentum equation and a “mass

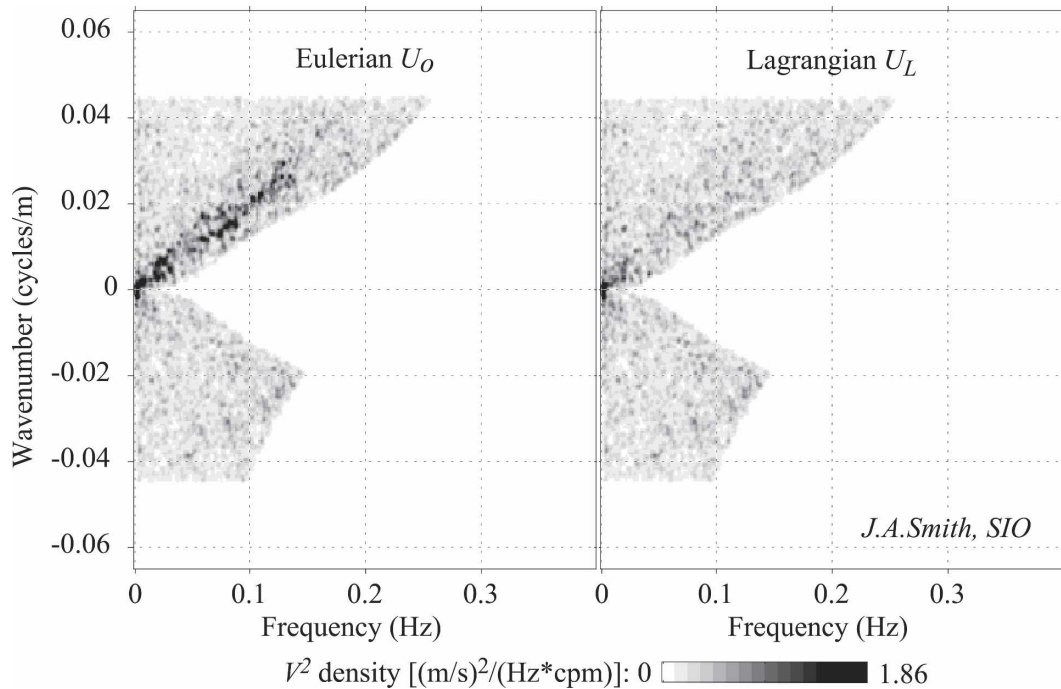


FIG. 15. Wavenumber–frequency spectra for (left) the Eulerian velocity field and (right) the Lagrangian velocity field formed by adding the Eulerian and Stokes drift estimates. The reduction in variance along the 5 m^{-1} line in the Lagrangian field is dramatic. Because the means are not well determined, some residual variance is to be expected near the origin. Comparison of the spectral levels at + and $-k$ values for the same frequencies confirms that there is little or no preferential direction for the Lagrangian variance (right). Elimination of the variance from the Lagrangian spectrum implies complete cancellation of the Stokes drift by the Eulerian response.

source” at the surface. Consider waves aligned with the x axis, having wavenumber k , and a regular group modulation with wavenumber K [e.g., for the simplest case of two wavenumbers k_1 and k_2 , let $k = (k_1 + k_2)/2$

and $K = (k_2 - k_1)$]. Let U be the surface value of the current associated with the induced motion. The near-surface momentum equation is

$$\partial_t U + \partial_x(U^2) + g\partial_x \bar{\zeta} = \rho^{-1} F^W, \tag{7.1}$$

where $\bar{\zeta}$ is the surface deflection associated with the response, ρ is the water density (assumed constant and set to one), and the wave force F^W is

$$\mathbf{F}^W \equiv B\mathbf{M}^W + \mathbf{M}^W \times (\nabla \times \mathbf{U}) - \mathbf{U}(\nabla \cdot \mathbf{M}^W) \tag{7.2}$$

(Garrett 1976; for an extension to the finite depth see Smith 1990). Here, $\mathbf{M}^W = \rho T^S$ is the wave momentum. In the first term, B represents a dissipation rate (e.g., by breaking). The second term is the return force resulting from refraction of the waves by the current, and the last accounts for mass transferred from the wave transport to the mean transport at speed U . Here U is assumed small, as is $U^S = 2kT^S$, and second-order terms are neglected [the second term in (7.1) and the last in (7.2)]. Breaking and vorticity are also neglected, so in this case the wave force is negligible. Under the same assumptions, the surface boundary condition is

$$\partial_t \bar{\zeta} - W = -\partial_x T^S, \tag{7.3}$$

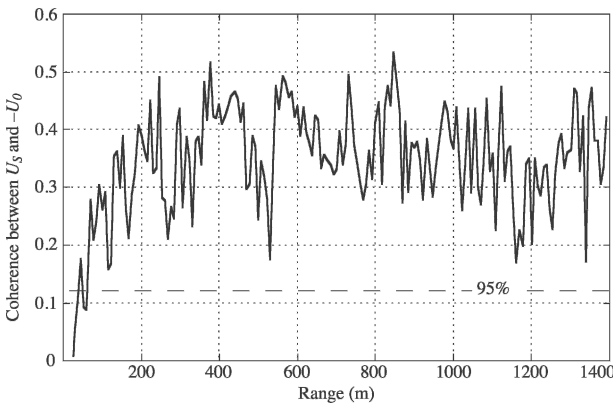


FIG. 16. Coherence between U_S and the wave-filtered Eulerian velocity $-U_0$ vs range, as estimated from time averages: $-\langle U_S U_0 \rangle / (\langle U_S^2 \rangle \langle U_0^2 \rangle)^{1/2}$ (note minus sign). The 95% level is about 0.12 (dashed line), and the coherence levels are more than twice this. The maximum coherence occurs with no spatial offset (i.e., no phase lag between U_S and U_0).

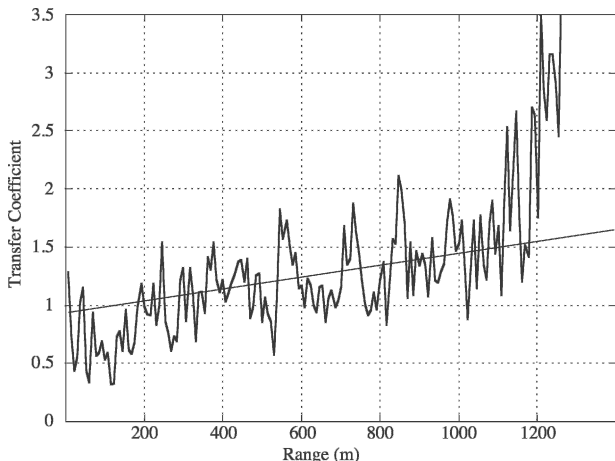


FIG. 17. The transfer coefficient from Stokes drift U_S to the negative Eulerian velocity anomaly (wave filtered) $-U_0$; $T_C = -\langle U_S U_0 \rangle / \langle U_S^2 \rangle$. This starts very near 1.0 at near ranges, indicating that the correlated part of the two fields cancel out. A value over 1 indicates a Eulerian anomaly larger than the Stokes drift, contrary to expectations. As range increases, the Stokes drift is probably underestimated slightly because of finite spatial smoothing. The increase in transfer coefficient with range is likely attributable to this, and might serve as a guide in compensating for this underestimation (see Fig. 11). The response is no smaller than the Stokes drift, and is most likely a one-to-one match, as also implied by the elimination of variance from the Lagrangian velocity spectrum (Fig. 15).

where W is the vertical velocity associated with the response (forced long wave). Thus, in deep water the long wave is forced entirely by mass conservation. For a wave group with envelope wavenumber K propagating with group speed c_g as contemplated here, ∂_t can be replaced by $-c_g \partial_x$ and the response should have a depth dependence of the form e^{Kz} (assuming, as seems reasonable, that the response is irrotational). At the surface, W can be replaced by $\partial_x(U/K)$ in this case (by continuity with integration). The momentum and the surface boundary condition reduce to

$$\partial_x(-c_g U + g\bar{\zeta}) = 0, \tag{7.4}$$

and

$$\partial_x(U/K - c_g \bar{\zeta} + T^S) = 0, \tag{7.5}$$

respectively. Choosing constants of integration so that $U = 0$ when $\bar{\zeta} = 0$, the results have the same form but with the partials dropped. The solution is

$$\bar{\zeta} = (c_g/g)U, \tag{7.6}$$

$$U = -\frac{gT^S}{g/K - c_g^2}. \tag{7.7}$$

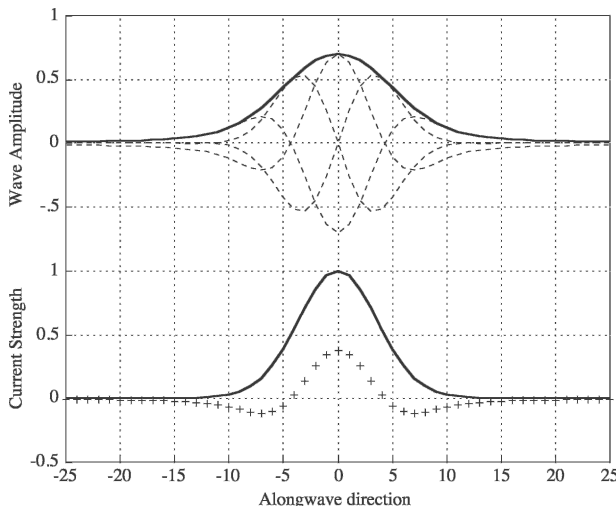


FIG. 18. (top) A conceptual minimal-length wave group, showing quadrature phase wave profiles (dashed) and an envelope (solid). (bottom) The resulting Stokes drift (solid line), and the calculated response from simple theory (+ symbols). Simple theory predicts the largest response for the shortest groups; even for this minimal-length group, the response is substantially below 1:1.

For deep-water waves, $c_g^2 = (1/2c)^2 = 1/4(g/k)$; using also $T^S = (2k)^{-1}U^S$, (7.7) can be written as

$$U = -U^S \left(\frac{2c_g^2}{g/K - c_g^2} \right) = -U^S \left[\frac{(K/2k)}{1 - (K/4k)} \right], \tag{7.8}$$

which is useful for comparison with the results of section 6. For compact groups, that is, as K decreases toward k , the factor in 7.8 increases toward $2/3$, but the estimated response U cannot get as large as $-U^S$, as is observed.

There is a kinematic constraint on the minimum group length in deep water: it must be long enough to maintain a constant mean elevation over the group for all phases of the wave. For example, a model minimum-length group is obtained by multiplying a Gaussian envelope times a trend, then forming the Hilbert transform to obtain the out-of-phase portion (Fig. 18). The resulting group has the ratio $K/k \approx 0.6$ (using spectral mean wavenumbers for both), and the calculated response peaks at $U \approx -0.4U^S$ [calculated from the spectrum of the group envelope using (7.8) for each component, as suggested originally by Longuet-Higgins and Stewart (1962)]. The overall response is substantially lower than 1:1.

From (7.8), there should be significant K dependence in the response. The factor involving K does not flatten out short of $K = 2k$, yet values of $K > k$ are unreasonable. For smaller K , there should be an approximately

linear increase in response with K . As seen in the k - f spectrum of the Eulerian and Lagrangian velocity fields, however (Fig. 15), there is no evidence of K dependence in the observed response. Rather, looking in particular at the estimated Lagrangian response, the Eulerian and Stokes drift fields appear to cancel at a one-to-one ratio across all the wavenumbers along the 5 m s^{-1} ridge (except perhaps at the lowest wavenumbers and frequencies, where the response is less well determined: the wave-induced motion of *FLIP* is removed via a full-field average, depending therefore on the ratio of the group size or response scale to the field of view, approximately 1 km).

This simple analysis has several weaknesses. First, no attempt is made to describe or reconcile the dynamics of a “minimum-length wave group.” Also, analysis is truncated at second order, whereas the waves at mid-group must be steep; this relates (in extreme form) to the effect of breaking, parameterized as BM^W in (7.2). Systematic breaking at the wave group maxima would have two effects: 1) the resultant wave-breaking force opposes the response velocity, so it would work to reduce the energy of the response, and 2) its integral is out of phase with the prior response, so it would alter the phase. Last, the separation of scales used to derive the above equations becomes invalid as the limit of minimal group length is approached. However, historically such simple two-scale analyses have proved surprisingly robust, perhaps because of the fundamental footing on the conservation of mass, momentum, and vorticity. They generally provide guidance on at least the qualitative behavior of the system, even near the limits of validity. Here, the fundamental driving term is mass conservation. To maintain an irrotational flow field, the response must be made up of irrotational and incompressible components (vorticity cannot be advected over several meters depth in the time it takes a single group to pass). The observations present a puzzle: the observed response is too large, even positing unreasonably short wave groups; further, the response ratio appears to be scale independent.

As noted in the introduction, Eulerian counterflows have also been observed in laboratory experiments (e.g., Groeneweg and Klopman 1998; also Kemp and Simons 1982, 1983; Swan 1990; Jiang and Street 1991; S. G. Monismith et al. 1996, unpublished manuscript). Both Groeneweg and Klopman (1998) and Huang and Mei (2003) have treated the problem using numerical generalized Lagrangian mean formulations (cf. Andrews and McIntyre 1978). However, these results pertain to statistically steady or slowly varying waves and flows, so the “group size” is large. The observed and calculated changes in profiles from case to case (no

waves, down-current waves, up-current waves) are approximately equal to the Stokes drift profiles calculated from the wave parameters as given. Because they treat the full problem, including shear, viscosity, and turbulence, the solution permits vorticity in the (quasi steady) response, which has time to diffuse downward through the system. In contrast, the short groups observed here are much too fast for diffusion of vorticity to occur; further, there is no phase lag in the response as that would seem to imply.

8. Results and conclusions

There are two significant scientific results:

- 1) As wave groups pass, Eulerian counterflows occur that cancel the Stokes drift variations at the surface.

The magnitude of this counterflow at the surface exceeds predictions based on an irrotational response (cf. Longuet-Higgins and Stewart 1962); namely, the response approaches 1/2–2/3 the surface Stokes drift as the wave group length decreases to a single wave. In contrast, the observed response is roughly 1:1 across the entire broad range of wavenumbers resolved. The mechanism by which this counterflow is generated is not well understood.

- 2) The Stokes drift resulting from open-ocean surface waves is highly intermittent.

While this is expected also with a Rayleigh distribution of wave amplitudes, appropriate to random seas (Longuet-Higgins 1969b), the observations also show compact wave “packets” (perhaps too short to be called “groups”) that appear to remain coherent for a considerable distance as they propagate. Such coherent packets have not been observed in open-ocean deep-water conditions previously. As an aside, it may be speculated that because the Eulerian response is of the same order as finite-amplitude dispersion corrections, it may be important in understanding wave group dynamics.

In addition, several technical issues have been addressed:

- 1) The difference between an area-mean velocity based on feature tracking and one based on area-mean Doppler shifts (so-called FDV) has been analyzed and explained in terms of the acoustic sheltering of wave crests. The sheltering of crests moves the measurements from being semi-Lagrangian (surface following) toward being more nearly at a fixed level. For the typical wave steepness, sonar depth, and range interval employed, the analysis suggests that about 1/4 of the Stokes drift remains in the mea-

sured Doppler means (as opposed to 1/2 for the semi-Lagrangian limit with no sheltering). The effect of a wind-drift layer contributes a small additional deficit to the measurements, making the FDV closer to the full value of Stokes drift (bringing it up to 92%, rather than 75%, as estimated here).

- 2) Including the FDV (as method 1), three methods were developed to estimate Stokes drift from the data. In particular, methods 2 and 3 permit estimation of the time-space trajectories of Stokes drift anomalies associated with wave groups, in a form directly comparable to that in which the underlying flow is measured. Method 2 makes use of weighted FFT coefficients on the k - f plane, and is efficient. Method 3 involves detailed extrapolation of the measured velocities to both a fixed level and the moving surface. While more computationally demanding, this also permits explicit estimation of both the Eulerian and fully Lagrangian velocity fields, and also of sheltering and drift current effects.
- 3) The spatial and temporal extent of the data permits aliased wave variance to be unwrapped in the spectral domain. This effectively extends the resolution of the wave measurements to include the entire portion of the wave spectrum thought most relevant to wave-current interaction dynamics (up to frequencies of order 0.3 Hz).

Acknowledgments. This work was supported by the ONR Physical Oceanography program (C/G N00014-02-1-0855). I thank J. Klymak, R. Guza, R. Pinkel, K. Melville, J. Polton, and many others for useful discussions and suggestions. A big thanks also is given to the OPG engineering team of E. Slater, M. Goldin, and M. Bui for their tireless efforts to design, construct, deploy, and operate the LRPADS and for helping to develop the software to analyze the resulting data. Thanks also are given to NSF for supporting the HOME field experiments, with which this project enjoyed significant synergy.

REFERENCES

- Andreas, E. L., J. B. Edson, E. C. Monahan, M. P. Rouault, and S. D. Smith, 1995: The spray contribution to net evaporation from the sea—A review of recent progress. *Bound.-Layer Meteor.*, **72**, 3–52.
- Andrews, D. G., and M. E. McIntyre, 1978: An exact theory of nonlinear waves on a Lagrangian mean flow. *J. Fluid Mech.*, **89**, 609–646.
- Asher, W. E., L. M. Karle, B. J. Higgins, P. J. Farley, E. C. Monahan, and I. S. Leifer, 1996: The influence of bubble plumes on air-seawater gas transfer velocities. *J. Geophys. Res.*, **101**, 12 027–12 041.
- Banner, M. L., and O. M. Phillips, 1974: On the incipient breaking of small scale waves. *J. Fluid Mech.*, **65**, 647–656.
- Brumley, B. H., R. G. Cabrera, K. L. Deines, and E. A. Terray, 1991: Performance of a broad-band acoustic Doppler current profiler. *IEEE J. Oceanic Eng.*, **16**, 402–407.
- Craik, A. D. D., 1977: The generation of Langmuir circulation by an instability mechanism. *J. Fluid Mech.*, **81**, 209–223.
- , and S. Leibovich, 1976: A rational model for Langmuir circulations. *J. Fluid Mech.*, **73**, 401–426.
- Crawford, C. B., and D. M. Farmer, 1987: On the spatial distribution of ocean bubbles. *J. Geophys. Res.*, **92**, 8231–8243.
- Edson, J. B., and C. W. Fairall, 1994: Spray droplet modeling. 1. Lagrangian model simulation of the turbulent transport of evaporating droplets. *J. Geophys. Res.*, **99**, 25 295–25 311.
- Garrett, C., 1976: Generation of Langmuir circulations by surface waves—A feedback mechanism. *J. Mar. Res.*, **34**, 117–130.
- Groeneweg, J., and G. Klopman, 1998: Changes of the mean velocity profiles in the combined wave-current motion described in a GLM formulation. *J. Fluid Mech.*, **370**, 271–296.
- Hara, T., and S. E. Belcher, 2002: Wind forcing in the equilibrium range of wind-wave spectra. *J. Fluid Mech.*, **470**, 223–245.
- Herbers, T. H. C., S. Elgar, and R. T. Guza, 1994: Infragravity-frequency (0.005–0.05 Hz) motions on the shelf. Part I: Forced waves. *J. Phys. Oceanogr.*, **24**, 917–927.
- Huang, Z. H., and C. C. Mei, 2003: Effects of surface waves on a turbulent current over a smooth or rough seabed. *J. Fluid Mech.*, **497**, 253–287.
- Jiang, J.-Y., and R. L. Street, 1991: Modulated flows beneath wind-ruffled, mechanically generated water waves. *J. Geophys. Res.*, **98**, 2711–2721.
- Kemp, P. H., and R. R. Simons, 1982: The interaction of waves and a turbulent current; waves propagating with the current. *J. Fluid Mech.*, **116**, 227–250.
- , and —, 1983: The interaction of waves and a turbulent current; waves propagating against the current. *J. Fluid Mech.*, **130**, 73–89.
- Kenyon, K. E., 1969: Stokes drift for random gravity waves. *J. Geophys. Res.*, **74**, 6991–6994.
- Langmuir, I., 1938: Surface motion of water induced by wind. *Science*, **87**, 119–123.
- Leibovich, S., 1977: Convective instability of stably stratified water in the ocean. *J. Fluid Mech.*, **82**, 561–581.
- , 1980: On wave-current interaction theories of Langmuir circulations. *J. Fluid Mech.*, **99**, 715–724.
- Li, M., K. Zahariev, and C. Garrett, 1995: Role of Langmuir circulation in the deepening of the ocean surface mixed layer. *Science*, **270**, 1955–1957.
- Longuet-Higgins, M. S., 1953: Mass transport in water waves. *Philos. Trans. Roy. Soc. London*, **A245**, 535–581.
- , 1969a: Action of a variable stress at the surface of water waves. *Phys. Fluids*, **12**, 737–740.
- , 1969b: On wave breaking and the equilibrium spectrum of wind generated waves. *Proc. Roy. Soc. London*, **A310**, 151–159.
- , and R. W. Stewart, 1960: Changes in the form of short gravity waves on long waves and tidal currents. *J. Fluid Mech.*, **8**, 565–583.
- , and —, 1961: The changes in amplitude of short gravity waves on steady non-uniform currents. *J. Fluid Mech.*, **10**, 529–549.
- , and —, 1962: Radiation stress and mass transport in gravity waves, with application to “surf-beats.” *J. Fluid Mech.*, **13**, 481–504.
- , and —, 1964: Radiation stresses in water waves—A physi-

- cal discussion, with applications. *Deep-Sea Res. Oceanogr. Abstr.*, **11**, 529–562.
- McWilliams, J. C., and P. P. Sullivan, 2000: Vertical mixing by Langmuir circulations. *Spill Sci. Technol. Bull.*, **6**, 225–237.
- , —, and C. H. Moeng, 1997: Langmuir turbulence in the ocean. *J. Fluid Mech.*, **334**, 1–30.
- Nepf, H. M., 1992: The production and mixing effects of Langmuir circulations. Ph.D. thesis, Stanford University.
- Pattison, M. J., and S. E. Belcher, 1999: Production rates of sea-spray droplets. *J. Geophys. Res.*, **104**, 18 397–18 407.
- Phillips, W. R. C., 2002: Langmuir circulations beneath growing or decaying surface waves. *J. Fluid Mech.*, **469**, 317–342.
- Pierson, W. J., and L. Moskowitz, 1964: A proposed spectral form for fully developed wind seas based on the similarity theory of S. A. Kitaigorodskii. *J. Geophys. Res.*, **69**, 5181–5190.
- Pinkel, R., and J. A. Smith, 1992: Repeat-sequence coding for improved precision of Doppler sonar and sodar. *J. Atmos. Oceanic Technol.*, **9**, 149–163.
- Plant, W. J., and J. Wright, 1980: Phase speeds of upwind and downwind travelling short gravity waves. *J. Geophys. Res.*, **85**, 3304–3310.
- Rudnick, D. L., and Coauthors, 2003: From tides to mixing along the Hawaiian Ridge. *Science*, **301**, 355–357.
- Rummler, W. D., 1968: Introduction of a new estimator for velocity spectral parameters. Rep. MM-68-4141-5, AT&T Bell Labs., Whippany, NJ, 24 pp.
- Skyllingstad, E. D., and D. W. Denbo, 1995: An ocean large-eddy simulation of Langmuir circulations and convection in the surface mixed layer. *J. Geophys. Res.*, **100**, 8501–8522.
- Smith, J. A., 1983: On surface gravity waves crossing weak current jets. *J. Fluid Mech.*, **134**, 277–299.
- , 1986: Short surface waves with growth and dissipation. *J. Geophys. Res.*, **91**, 2616–2632.
- , 1990: Modulation of short wind waves by long waves. *Surface Waves and Fluxes: Current Theory and Remote Sensing*, G. L. Geernaert and W. J. Plant, Eds., Kluwer Academic, 247–284.
- , 1992: Observed growth of Langmuir circulation. *J. Geophys. Res.*, **97**, 5651–5664.
- , 1998: Evolution of Langmuir circulation during a storm. *J. Geophys. Res.*, **103**, 12 649–12 668.
- , 2002: Continuous time–space sampling of near-surface velocities using sound. *J. Atmos. Oceanic Technol.*, **19**, 1860–1872.
- , and G. T. Bullard, 1995: Directional surface wave estimates from Doppler sonar data. *J. Atmos. Oceanic Technol.*, **12**, 617–632.
- Stokes, G. G., 1847: On the theory of oscillatory waves. *Trans. Cambridge Philos. Soc.*, **8**, 441–455.
- Sullivan, P. P., J. C. McWilliams, and W. K. Melville, 2004: The oceanic boundary layer driven by wave breaking with stochastic variability. Part 1. Direct numerical simulations. *J. Fluid Mech.*, **507**, 143–174.
- Swan, C., 1990: Convection within an experimental wave flume. *J. Hydraul. Res.*, **28**, 273–282.
- , I. P. Cummins, and R. L. James, 2001: An experimental study of two-dimensional surface water waves propagating on depth-varying currents. Part 1. Regular waves. *J. Fluid Mech.*, **428**, 273–304.
- Terray, E. A., M. A. Donelan, Y. C. Agrawal, W. M. Drennan, K. K. Kahma, A. J. Williams, P. A. Hwang, and S. A. Kitaigorodskii, 1996: Estimates of kinetic energy dissipation under breaking waves. *J. Phys. Oceanogr.*, **26**, 792–807.
- Theriault, K. B., 1986: Incoherent multibeam Doppler current profiler performance. Part I: Estimate variance. *IEEE J. Oceanic Eng.*, **11**, 7–15.
- Thompson, R. O. R. Y., 1979: Coherence significance levels. *J. Atmos. Sci.*, **36**, 2020–2021.
- Thorpe, S. A., 1982: On the clouds of bubbles formed by breaking wind waves in deep water, and their role in air-sea gas transfer. *Philos. Trans. Roy. Soc. London*, **A304**, 155–210.
- , 1986: Bubble clouds: A review of their detection by sonar, of related models, and of how K_v may be determined. *Oceanic Whitecaps and Their Role in Air-Sea Exchange Processes*, E. C. Monahan and G. M. Niocaill, Eds., D. Reidel, 57–68.
- Trevorrow, M. V., and D. M. Farmer, 1992: The use of Barker codes in Doppler sonar measurements. *J. Atmos. Oceanic Technol.*, **9**, 699–704.
- Wu, J., 1975: Wind-induced drift currents. *J. Fluid Mech.*, **68**, 49–70.
- Zappa, C. J., W. E. Asher, A. T. Jessup, J. Klinke, and S. R. Long, 2004: Microbreaking and the enhancement of air-water transfer velocity. *J. Geophys. Res.*, **109**, C08S16, doi:10.1029/2003JC001897.
- Zilitinkevich, S. S., A. A. Grachev, and C. W. Fairall, 2001: Scaling reasoning and field data on the sea surface roughness lengths for scalars. *J. Atmos. Sci.*, **58**, 320–325.